

This represents a post-print of a peer-reviewed manuscript that has been accepted for publication in *Geochemistry, Geophysics, Geosystems* (acceptance date 19/10/2021).

1 **This manuscript has been accepted for publication in *Geochemistry,***
2 ***Geophysics, Geosystems.* The published version of the manuscript**
3 **can be found here:**

4 <https://doi.org/10.1029/2020GC009560>

5

6 **Please cite this manuscript as:**

7 Gleeson, M., and Gibson, S. (2021). Insights into the nature of plume-ridge interaction and
8 outflux of H₂O from the Galápagos Spreading Centre. *Geochemistry, Geophysics,*
9 *Geosystems.* e2020GC009560. <https://doi.org/10.1029/2020GC009560>

10

11 **Insights into the nature of plume-ridge interaction**
12 **and outflux of H₂O from the Galápagos Spreading**
13 **Centre**

14

15 Matthew L. M. Gleeson^{1,2*} and Sally A. Gibson¹

16 ¹Department of Earth Sciences, University of Cambridge, Downing Street, Cambridge, UK, CB2 3EQ.

17 ²School of Earth and Environmental Sciences, Cardiff University, Park Place, Cardiff, CF10 3AT, UK

18 Corresponding author email: gleesonm1@cardiff.ac.uk

19 **KEY POINTS**

- 20 1. Basalts erupted on segments of the global ridge system adjacent to the Galapagos mantle
21 plume have high volatile (H₂O & F) contents.
- 22 2. Channelised melt transport between the Galápagos mantle plume stem and the GSC causes
23 variations in crustal thickness and geochemistry.
- 24 3. Plume-derived volatile-rich melts contribute up to 20 – 60% of the total H₂O outflux at the
25 Galápagos Spreading Centre.

26 ABSTRACT

27 The flow of high-temperature and compositionally-enriched material between mantle plumes and
28 nearby spreading centres influences up to 30% of the global mid-ocean ridge system and represents
29 a significant, but currently unconstrained, flux of volatiles out of the mantle. Here we present new
30 analyses of H₂O, F, Cl and S in basaltic glass chips from an archetypal region of plume-ridge
31 interaction, the Galápagos Spreading Centre (GSC). Our dataset includes samples from the eastern
32 GSC, on ridge segments that are strongly influenced by the adjacent Galápagos mantle plume, and
33 complements published analyses of volatiles largely from the western GSC. We use forward models
34 of mantle melting to investigate the role of solid and melt-phase transport from a lithologically
35 heterogeneous (peridotite-pyroxenite) mantle in plume-ridge interaction along approximately 1000
36 km of the GSC. Our results indicate that the observed geochemical and geophysical variations cannot
37 be recreated by models which only involve solid-state transfer of material between the Galápagos
38 mantle plume and the GSC. Instead, we show that the geochemical and geophysical data from the
39 GSC are well-matched by models that incorporate channelised flow of volatile-rich melts formed at
40 high-pressures (>3 GPa) in the Galápagos plume stem to the GSC. In addition, our new models
41 demonstrate that channelised flow of enriched, plume-derived melt can account for up to ~60% of
42 the H₂O outgassed from regions of the GSC which are most strongly influenced by the Galápagos
43 mantle plume.

44 PLAIN LANGUAGE SUMMARY

45 Approximately one-third of Earth's global mid-ocean ridge system is influenced by the transfer of
46 compositionally distinct material from nearby upwellings of anomalously hot mantle. Transfer of this
47 plume material to oceanic spreading centres might represent an important mechanism of volatile
48 loss from Earth's mantle, but there are limited constraints on the quantities of H₂O and other

This represents a post-print of a peer-reviewed manuscript that has been accepted for publication in *Geochemistry, Geophysics, Geosystems* (acceptance date 19/10/2021).

49 volatiles that degas from these plume-influenced spreading centres. In this study, we evaluate the
50 mechanism of plume-ridge interaction between the Galápagos mantle plume and the nearby
51 Galápagos Spreading Centre (GSC) using new analyses of volatiles in basalts erupted on the ridge.
52 The results from new numerical models demonstrate that the geochemical and geophysical
53 signatures of plume-ridge interaction along the GSC are best explained if the transport of deep
54 sourced mantle material between the Galápagos mantle plume and GSC occurs in the melt phase
55 rather than as a solid. In addition, our new analyses enable us to constrain the flux of H₂O out of the
56 GSC and demonstrate that melt channelization can account for up to ~60% of the H₂O flux out of
57 plume-influenced ridges.

58 1 INTRODUCTION

59 The majority of ocean island basalts (OIBs) are believed to form as a consequence of adiabatic
60 decompression melting in high-temperature, and potentially lithologically-heterogeneous, mantle
61 plumes (Asimow and Langmuir, 2003; Herzberg and Asimow, 2008; Ito and Mahoney, 2005; Métrich
62 et al., 2014; Morgan, 1971; Sobolev et al., 2007). Higher concentrations of volatiles (such as H₂O, F,
63 or Cl) in OIBs compared to mid-ocean ridge basalts (MORBs) reflect the volatile-rich nature of deep-
64 sourced plume material, relative to the MORB source, and are evidence of small-fraction
65 decompression melting at higher pressures than the anhydrous peridotite solidus (Dixon et al., 2017;
66 Gibson and Richards, 2018; Ingle et al., 2010; Jackson et al., 2015; Koleszar et al., 2009; Métrich et
67 al., 2014). In addition, approximately 30% of the global mid-ocean ridge (MOR) system is influenced
68 by the lateral transfer of deep-sourced mantle plume material (Ito and Lin, 1995) and potentially
69 represent sites of substantial volatile outgassing from the Earth's mantle (Gibson and Richards,
70 2018; Le Voyer et al., 2018). Nevertheless, robust estimates for the outflux of volatiles from mantle
71 plume influenced segments of MORs are rare. In addition, there remain outstanding issues related to

This represents a post-print of a peer-reviewed manuscript that has been accepted for publication in *Geochemistry, Geophysics, Geosystems* (acceptance date 19/10/2021).

72 the role of melt channelisation in the transfer of geochemically enriched plume material between
73 mantle plume stems and nearby spreading centres.

74 Over the past few decades, numerous hypotheses have been put forward to explain both the long
75 and short length-scale geochemical and geophysical heterogeneities that are observed along plume-
76 influenced regions of the global MOR system. These previously proposed hypotheses include: (i)
77 buoyancy-driven upwelling of solid peridotite beneath ridge segments that are most strongly
78 influenced by nearby mantle plumes (e.g. Ingle et al., 2010; MacLennan et al., 2001; Sleep, 1990); (ii)
79 radial spreading of solid plume material, consisting of enriched blebs embedded in a depleted matrix
80 (and the role of these enriched components in dynamic plume flow; Bianco et al., 2013; Ito and
81 Bianco, 2014; Ito and Mahoney, 2005; Ribe, 1996; Shorttle et al., 2010); (iii) flow of solid plume
82 material in a sub-lithospheric channel (Morgan, 1978; Schilling et al., 1982); (iv) melt transport via
83 porous flow at the base of the lithosphere (Braun and Sohn, 2003); and (v) channelized buoyancy-
84 driven flow of off-axis plume-derived melts in a matrix of dispersing solid plume material (Gibson et
85 al., 2015; Gibson and Richards, 2018; Mittal and Richards, 2017; Stroncik et al., 2008; Stroncik and
86 Devey, 2011).

87 Channelised, buoyancy-driven flow of volatile-rich melts in a network of channels embedded in a
88 spreading 'puddle' of solid plume material (hypothesis (v) above) was first put forward by Gibson et
89 al. (2015) to account for the simultaneous presence of enriched basalts on the GSC and depleted
90 basalts found in nearby regions of the northeast Galápagos Archipelago (e.g. Genovesa).

91 Subsequently, Mittal and Richards (2017) and Gibson and Richards (2018) extended this conceptual
92 model to account for certain enigmatic features at global sites of plume-ridge interaction (including
93 the Galápagos, the Azores, Discovery, and Reunion), such as the coincidence of the intersection of
94 non-age progressive volcanic lineaments with excess crustal thickness and short length-scale
95 geochemical anomalies (i.e. highly-enriched basalts) on the spreading ridge.

96 Despite continued development in the conceptual models of plume-ridge interaction via a network
97 of melt channels embedded in solid plume material, a focused geochemical study on the role of
98 channelised volatile-rich melts to an individual spreading centre has yet to be undertaken. Here, we
99 present new volatile data (H₂O, F, Cl and S) for basaltic glass chips from plume-influenced segments
100 of the GSC, including the eastern GSC where only limited volatile data previously existed (e.g. Byers
101 et al., 1983). We use our new and published volatile data in combination with forward melting
102 models to evaluate whether plume-ridge interaction via channelised flow of volatile-rich melts
103 derived from a pyroxenitic source component in a mixed peridotite-pyroxenite mantle can explain
104 the long (100s of km) and short (10s of km) length-scale heterogeneities observed in basalt
105 chemistry and crustal thickness at this single site of plume-ridge interaction. Our new volatile data
106 and forward models of mantle melting also allow us to estimate the outflux of H₂O from the entire
107 region of Galápagos plume-influenced ridge.

108 2 GEOLOGICAL BACKGROUND

109 2.1 MANTLE HETEROGENEITY

110 Located ~1000 km off the western coast of Ecuador, the Galápagos Archipelago represents a well-
111 known example of mantle plume related volcanism (Morgan, 1978). Active and recent Holocene
112 volcanism is observed over a wide geographic area and geochemical studies of both subaerial and
113 submarine basaltic lavas reveal that compositional heterogeneity results from the melting of at least
114 4 isotopically-distinct components in the Galápagos mantle plume (Geist et al., 1998; Harpp and
115 Weis, 2020; Harpp and White, 2001; Hoernle et al., 2000; White and Hofmann, 1978; White et al.,
116 1993). The isotopic end-members of the Galápagos mantle plume include an isotopically depleted
117 component and 3 isotopically enriched mantle components, that can be summarised as:

- 118 1. PLUME component - dominant in basalts from the western Galápagos Archipelago (centred
119 on Isla Fernandina), which are characterised by moderately enriched Sr, Nd and Pb isotope

This represents a post-print of a peer-reviewed manuscript that has been accepted for publication in *Geochemistry, Geophysics, Geosystems* (acceptance date 19/10/2021).

120 ratios and elevated $^3\text{He}/^4\text{He}$ ratios ($\sim 30 R/R_A$; Harpp and White, 2001; Kurz et al., 2009; Kurz
121 and Geist, 1999). The isotopic signatures of the PLUME component resembles the 'FOZO' or
122 'C' global mantle end-member (Hanan and Graham, 1996; Hart et al., 1992).

123 2. Floreana (FLO) component – centred on the southern island of Floreana and characterised
124 by the most radiogenic Sr and Pb isotope signatures observed anywhere in the Galápagos
125 (Harpp et al., 2014a; Harpp and White, 2001). The FLO component is hypothesised to result
126 from melting of ancient recycled oceanic crust ($\sim 2.2 - 2.5$ Ga) incorporated into the
127 Galápagos plume (Gibson et al., 2016; Harpp et al., 2014a).

128 3. Wolf-Darwin (WD) component – most prevalent in basaltic lavas from the northern islands
129 of Pinta, Wolf, Darwin and surrounding seamounts (Harpp et al., 2014c; Harpp and White,
130 2001). The WD component is characterised by elevated $^{208}\text{Pb}/^{206}\text{Pb}$ and $^{207}\text{Pb}/^{206}\text{Pb}$ ratios
131 (Harpp and White, 2001). The origin of this component remains enigmatic.

132 The spatial heterogeneity in the radiogenic isotope composition of basalts erupted in the Galápagos
133 Archipelago provides insights into the structure of the underlying plume and the deep mantle. For
134 example, isotopically enriched signatures are most commonly observed in the south-western
135 Archipelago (corresponding to the PLUME and FLO components), whereas isotopically depleted
136 basalts are typically found further east (Harpp and Weis, 2020; Harpp and White, 2001; Hoernle et
137 al. 2000; White and Hofmann, 1978; White et al., 1993). This bilateral asymmetry in the composition
138 of the upwelling mantle plume, which is similar to that observed in Hawaii and other regions of
139 plume-derived volcanism worldwide (Harpp et al., 2014b; Weis et al., 2011), has been linked to the
140 presence of deep mantle superstructures at the base of the Galápagos plume (Gleeson et al., 2021;
141 Harpp and Weis, 2020). Specifically, the isotopically-enriched signatures of the south-western
142 Galápagos have been assigned to melting of material originating in the Pacific Large Low Shear
143 Velocity Province, whilst the isotopically-depleted signatures of the eastern Galápagos volcanoes are
144 assigned to melting of the ambient Pacific lower mantle or entrained upper mantle material (Harpp

This represents a post-print of a peer-reviewed manuscript that has been accepted for publication in *Geochemistry, Geophysics, Geosystems* (acceptance date 19/10/2021).

145 and Weis, 2020). This simple picture of mantle isotopic heterogeneity in the Galápagos plume is
146 complicated by the non-trivial relationship between isotopic and lithological heterogeneity. Olivine
147 minor element concentrations were originally used to indicate that both isotopically-enriched and
148 isotopically-depleted pyroxenite components are present in the Galápagos mantle plume (Vidito et
149 al., 2013). However, recent models that consider the influence of magma chamber recharge on the
150 minor element contents of magmatic olivines suggest that basalts sourced from the isotopically-
151 depleted mantle component in the Galápagos plume are predominantly derived from a peridotitic
152 source (Gleeson and Gibson, 2019). Nevertheless, variations in the Fe-isotope composition of the
153 GSC basalts indicate that both peridotite and pyroxenite source components might contribute to the
154 composition of plume-influenced basalts on the GSC (Gleeson et al., 2021, 2020).

155 2.2 GEOPHYSICAL AND GEOCHEMICAL HETEROGENEITY ALONG THE GSC

156 The Galápagos Spreading Centre separates the Cocos and Nazca tectonic plates and lies ~150-250
157 km north of the centre of Galápagos plume upwelling, at 100 km depth, that has been postulated
158 from seismic tomography (Fig. 1; Hooft et al., 2003; Villagómez et al., 2014). This lies to the north-
159 east of the postulated location of the plume stem at 200 km depth, i.e. beneath southern Isabela.
160 Variations in crustal thickness and ridge morphology provide evidence for the influence of the
161 Galápagos mantle plume along a ~1000 km wide zone of the GSC, extending between 85.5°W and
162 95.5°W (e.g. Christie et al., 2005; Ito and Lin, 1995). For example, a crustal thickness high is observed
163 at ~90.5 °W, near the closest point on the GSC to the centre of the mantle plume upwelling (Canales
164 et al., 2002; Christie et al., 2005; Detrick et al., 2002; Mittelstaedt et al., 2014).

165 Several features observed along both the eastern and western GSC, which are separated by a major
166 transform fault at ~91°W (the Galápagos Transform fault - GTF; Fig. 1), are consistent with a
167 decrease in magma supply with increasing distance from the mantle plume (Canales et al., 2014). For
168 example, changes in ridge morphology, from a low-relief valley and ridge terrain to a prominent
169 axial ridge, are observed on both ridge segments as the separation distance between the ridge and

170 hotspot decreases (Christie et al., 2005; Sinton et al., 2003). Additionally, along the western GSC the
171 depth of the seismically-imaged magma lens increases from 1-2.5 km east of 92.5°W to 2.5-4.5 km
172 between 92.7°W and 94.7°W, corresponding to a change from fissure-fed eruptions near the GTF to
173 point source eruptions further west (Behn et al., 2004; Blacic et al., 2004).

174 A prominent geochemical anomaly has been observed on the GSC near the GTF, between 89.5°W
175 and 92.5°W (Christie et al., 2005; Ingle et al., 2010; Schilling et al., 2003). Basalts erupted within this
176 region are characterised by elevated concentrations of strongly incompatible trace elements (e.g.
177 Nb, La) together with radiogenic Sr and Pb and unradiogenic Nd and Hf isotope ratios (Christie et al.,
178 2005; Gleeson et al., 2020; Ingle et al., 2010; Schilling et al., 2003, 1982). Many incompatible trace
179 element ratios (such as Sm/Yb and Nb/Zr) display broadly symmetric profiles that are centred
180 around ~91 – 91.5 °W, just to the west of the GTF (Fig. 1). In addition, positive correlations between
181 the large variations in incompatible trace element enrichment and Fe-isotopes in the GSC basalts
182 imply that the plume-influenced GSC basalts may be formed through melting of a lithologically-
183 heterogeneous mantle source (Gleeson et al., 2020).

184 Some important differences exist between the eastern and the western GSC. Firstly, the highest
185 resolution gravity and multi-beam bathymetry data available indicates that crustal thickness
186 increases by ~1 km from west to east across the GTF (Mittelstaedt et al., 2014). Secondly, the
187 eastern GSC basalts generally have lower ratios of fluid-mobile to fluid-immobile trace elements (e.g.
188 Ba/Nb; Fig. 1) and lower $^{208}\text{Pb}/^{204}\text{Pb}$ and $^{207}\text{Pb}/^{204}\text{Pb}$ ratios than basalts from the western GSC (e.g.
189 Christie et al., 2005; Gibson et al., 2015; Ingle et al., 2010; Schilling et al., 2003). The long length-
190 scale east-to-west geochemical differences on the GSC have been attributed to an additional
191 contribution of melts from the isotopically-enriched Wolf-Darwin Galápagos mantle component
192 beneath the western GSC (Gibson et al., 2015; Ingle et al., 2010; Schilling et al., 2003).

193 Gibson and Richards (2018) observed a series of short length-scale geochemical and geophysical
194 features that are superimposed on the broad length-scale heterogeneity of the GSC. For example,

195 basalts with anomalously high H₂O contents relative to their neighbouring basalts (typically >0.4
196 wt.%), and short length-scale crustal thickness anomalies occur at locations where long-lived
197 volcanic lineaments intersect the GSC (Mittelstaedt et al., 2014; Sinton et al., 2003). As a result, it
198 has been suggested that melt channels embedded within the 'normal' spreading of Galápagos plume
199 material may represent an important component of plume-ridge interaction (Gibson and Richards,
200 2018; Mittal and Richards, 2017). In this study, we use new melting models to critically evaluate the
201 role of both a mixed peridotite-pyroxenite mantle and melt channelisation from the Galápagos
202 plume stem in generating short and long length-scale geochemical and geophysical heterogeneities
203 on the GSC. In addition, our new data expands the existing volatile dataset for the GSC and enables
204 us to place improved constraints on the flux of H₂O out of the entire segment of plume-influenced
205 ridge.

206 3 METHODOLOGY

207 Twenty-two chips of basaltic glass (1-10 mm diameter) collected between 83 and 98°W on the
208 Galápagos Spreading Centre were selected from the Jean-Guy Schilling collection at the University of
209 Rhode Island, USA. Here we present new analyses of their H₂O, F, Cl, and S concentrations (Fig. 1).

210 The major and trace element contents of the selected glasses, together with their Fe, Sr, Nd, Hf, and
211 Pb isotope ratios, have previously been reported (Schilling et al., 2003; Gleeson et al., 2020). We
212 primarily selected samples from the eastern GSC for this analysis, as only limited volatile data
213 previously existed in this region, but a small number of samples (n=6) were chosen from the western
214 GSC to check that our results are consistent with previous studies (e.g., Cushman et al. 2004; Ingle et
215 al., 2010).

216 Basaltic glass chips in polished epoxy mounts were analysed for sulfur on a Cameca SX100 EPMA in
217 the Department of Earth Sciences at the University of Cambridge. Sulfur was analysed alongside
218 major elements (following methods described in Gleeson et al., 2020) to calculate the required

This represents a post-print of a peer-reviewed manuscript that has been accepted for publication in *Geochemistry, Geophysics, Geosystems* (acceptance date 19/10/2021).

219 matrix correction. The S concentrations were determined by counting for 90 s on the K_{α} peak using a
220 beam current of 10 nA, an acceleration voltage of 15 kV, and a defocussed beam (10 μm). Data
221 quality was checked using the VG2 basaltic glass standard (Jarosewich et al., 1980).

222 Prior to analysis of H_2O , F, and Cl on a Cameca ims-4f at the NERC Edinburgh Ion Microprobe Facility
223 (EIMF), the GSC glasses were briefly re-ground and polished, to remove topography caused by prior
224 laser ablation analysis, and gold coated. Secondary Ion Mass Spectrometry (SIMS) analysis was
225 carried out using a $^{16}\text{O}^-$ primary ion beam and a 14.5 keV net impact energy (4.5 keV secondary ion
226 accelerating voltage). A liquid nitrogen cold trap was used to reduce background counts on volatile
227 elements during analysis. Both static and electrostatic magnets were applied to centre H^+ ion images
228 relative to heavier masses. A 3 minute, 20 μm square raster pre-sputter was applied to reduce H^+
229 background. Analysis was then carried out using a 15-20 μm spot. Secondary ions were analysed
230 with a 25 μm image field. Analysis of quartz crystals at regular intervals during analysis was used to
231 determine H^+ backgrounds (< 0.02 wt%).

232 The SIMS data was collected over 8 cycles with total count times of 30 s for ^1H and 80 s for ^{19}F , 40s
233 for ^{35}Cl , and 16s for ^{30}Si , which was used for internal standardisation. ^1H counts were only recorded
234 for the final 6 cycles to avoid any contamination. H_2O concentrations for the GSC glasses were
235 calculated using a H_2O versus $^1\text{H}/^{30}\text{Si}$ calibration slope determined using analyses of BCR-2g
236 (anhydrous) and standards St-1, St-2, and St-6 from Shishkina et al. (2010). Calibration slopes for F
237 and Cl (F versus $^{19}\text{F}/^{30}\text{Si} \times \text{SiO}_2$ and Cl versus $^{35}\text{Cl}/^{30}\text{Si} \times \text{SiO}_2$) were determined using the composition
238 of BCR-2g from Marks et al. (2017). The 2σ analytical precision for H_2O (3.5%), F (8%) and Cl (16%)
239 was constrained using five repeat measurements of GSC basalt TR164 11D-1g.

240 4 RESULTS

241 Our new SIMS and EPMA data represent the first systematic analyses of H_2O , F, S and Cl for well-
242 characterised D-, N- and E-MORB erupted on the eastern GSC (geochemical divisions are the same as

243 those used in Gleeson et al. 2020), and thus expands the published volatile dataset to cover the
244 entire section of the Galápagos plume-influenced ridge (Cushman et al., 2004; Ingle et al., 2010; Le
245 Voyer et al., 2018; Michael, 1995).

246 **4.1 DEGASSING, CONTAMINATION AND FRACTIONAL CRYSTALLISATION**

247 The volatile contents of oceanic basalts are highly susceptible to modification by degassing,
248 contamination and crystal fractionation (Dixon, 1997; Kendrick et al., 2015; Workman et al., 2006).
249 All of the GSC samples analysed in this study were collected at water depths >1500 m and erupted
250 under high enough pressure to minimise loss of H₂O to a vapour phase (Dixon, 1997; Iacovino et al.,
251 2020; Shishkina et al., 2014). As a result, we estimate that degassing had only a minor influence on
252 the H₂O content of these GSC basalts (generally <2% loss; see Supplementary Information).

253 An indication of the extent of magmatic interaction with seawater or hydrothermal brines, which
254 can substantially influence the H₂O contents measured in submarine basalts (Kendrick et al., 2015),
255 is provided by the Cl and K₂O concentrations of basaltic lavas. In the GSC basalts, Cl exhibits a large
256 range (9 ppm to 3360 ppm) and almost all samples have Cl/K ratios that are much greater than those
257 previously proposed for primary OIBs or MORBs (Fig. 2a; 0.01-0.08, with some regions up to 0.15;
258 Kendrick et al., 2015; Le Roux et al., 2006; Michael and Cornell, 1998). We therefore suspect that
259 GSC basalts have assimilated a Cl-rich component (that is, a brine).

260 We used the H₂O/Cl, K/Cl and F/Cl ratios of the GSC basalts, together with an assumed Cl/K ratio of
261 0.08, to evaluate and correct for the effects of brine assimilation on their H₂O contents (see
262 Supplementary Information). Owing to the influence of brine assimilation on the Cl content of the
263 GSC basalts, we do not attempt to constrain variations in the Cl/K or Cl/Nb ratio of their mantle
264 source regions. Likewise, although S is commonly hypothesised to behave similarly to Dy during
265 mantle melting (Fig. 2b; Peterson et al., 2017), recent studies have shown that concentrations of
266 chalcophile elements (such as Se, Ag, and Cu) are required to truly evaluate the behaviour of S
267 during mantle melting and fractional crystallisation (Reekie et al., 2019; Sun et al., 2020; Wieser et

268 al., 2020). Since chalcophile element data is not available for our samples, we focus on constraining
269 only the H₂O and F systematics of the GSC mantle source regions.

270 To account for sub-ridge magma chamber processes, we have corrected the volatile data from the
271 GSC basalts for fractional crystallisation (to 8 wt. % MgO), using the method outlined for major and
272 trace elements by Gleeson et al. (2020) and mineral-melt volatile element partition coefficients
273 published by Hauri et al. (2006) and Johnson (2006).

274 4.2 VARIATIONS IN H₂O AND F CONTENTS OF GSC BASALTS

275 Our new SIMS data reveal that basalts from the GSC exhibit large variations in H₂O, with basalts from
276 the western GSC reaching higher concentrations (0.10 to 1.08 wt.%; Cushman et al., 2004) than
277 those on the eastern GSC (0.12 to 0.87 wt.%); this is a significant difference given the relatively small
278 analytical uncertainty of the H₂O analyses (predicted analytical error typically <<0.04 wt%). Fluorine
279 contents also show large variations in the GSC basalts; as with H₂O, F concentrations display a larger
280 range in basalts from the western GSC (70 – 838 ppm; Ingle et al., 2010) compared to the eastern
281 GSC (92 – 579 ppm). The highest concentrations of both H₂O (>0.4 wt.%) and F (>300 ppm) typically
282 occur in basalts erupted between 89 and 92 °W (i.e. on either side of the Galápagos Transform Fault,
283 Fig. 1), except for a single sample (ST7 17D-1g) collected from 86.13°W on the eastern GSC
284 (bathymetry data shows no evidence for a seamount or other topographic anomalies in this region;
285 Ryan et al., 2009). Our new data collected from the western GSC displays comparable H₂O and F
286 contents to similarly enriched samples previously analysed by Ingle et al. (2010) and Cushman et al.
287 (2004), and confirms that our analyses are consistent with those from these previous studies.

288 Both H₂O and F exhibit strong positive correlations with indices of trace element enrichment (such as
289 [La/Sm]_n) in the GSC basalts (Fig. 3; Supplementary Information). Importantly, the GSC basalts with
290 the highest H₂O and F contents (ST7 17D-1g and TR164 26D-3g) also have anomalously high δ⁵⁶Fe
291 values (Gleeson et al., 2020; Fig. 3). While Sr, Nd or Pb isotope data are not available for ST7 17D-1g,

292 we note that the volatile-rich sample TR164 26D-3g (90.95 °W) has enriched $^{87}\text{Sr}/^{86}\text{Sr}$, $^{143}\text{Nd}/^{144}\text{Nd}$
293 and Pb isotopic ratios relative to other GSC basalts.

294 5 CONSTRAINING THE VOLATILE CONTENT OF THE GSC MANTLE SOURCE

295 A common method for determining the volatile concentrations in the mantle source region of
296 oceanic basalts is to measure ratios of volatile and non-volatile trace elements that exhibit similar
297 incompatibilities during melting and crystal fractionation (Cabral et al., 2014; Jackson et al., 2015;
298 Koleszar et al., 2009; Michael, 1999; Saal et al., 2002). Widely used ratios include $\text{H}_2\text{O}/\text{La}$, $\text{H}_2\text{O}/\text{Ce}$,
299 F/Nd , Cl/K and S/Dy (Cabral et al., 2014; Jackson et al., 2015; Koleszar et al., 2009; Peterson et al.,
300 2017; Saal et al., 2002) although others have been suggested (e.g. F/Zr ; Le Voyer et al., 2015). In this
301 study we use the ratios $\text{H}_2\text{O}/\text{La}$ and F/Nd to describe the volatile systematics of the different
302 potential mantle components beneath the GSC (i.e. peridotite and pyroxenite). That is because,
303 recent constraints from experiments at mantle conditions on the mineral-melt partitioning of H_2O
304 and F (Dalou et al., 2012; Rosenthal et al., 2015), combined with new models of adiabatic
305 decompression melting, indicate that H_2O displays similar compatibilities to La during melting of
306 both peridotite and pyroxenite source components (see Supplementary Information; H_2O
307 partitioning data taken from Rosenthal et al. 2015). Fluorine is slightly less compatible than Nd
308 during melting of a pyroxenitic source lithology and slightly more compatible during melting of a
309 peridotitic source component (Supplementary Information; F partitioning data taken from Dalou et
310 al. 2012). These results are consistent with observations from global MORBs and OIBs (e.g.,
311 Danyushevsky et al., 2000; Kendrick et al., 2017).

312 The $\text{H}_2\text{O}/\text{La}$ ratios of the GSC basalts exhibit a negative correlation with indices of geochemical
313 enrichment (such as $[\text{La}/\text{Sm}]_n$; Fig. 2c). Variations in the $[\text{La}/\text{Sm}]_n$ ratio of the GSC basalts could,
314 theoretically, result from changes in the melt fraction of the mantle source; however, our mantle
315 melting models indicate that the negative correlation between $\text{H}_2\text{O}/\text{La}$ and $[\text{La}/\text{Sm}]_n$ is inconsistent

This represents a post-print of a peer-reviewed manuscript that has been accepted for publication in *Geochemistry, Geophysics, Geosystems* (acceptance date 19/10/2021).

316 with that predicted for melting of a single mantle source, as H₂O is slightly less compatible than La
317 during large amounts of mantle melting (Supplementary Information; Rosenthal et al., 2015). In
318 addition, as the [La/Sm]_n ratios of the GSC basalts have previously been shown to correlate with
319 radiogenic and stable isotope ratios (Schilling et al. 2003; Gleeson et al. 2020), we suggest that the
320 H₂O/La ratio of the GSC basalts is controlled by mixing of melts from multiple, lithologically-distinct
321 mantle components. Using the range of H₂O/La ratios measured in plume-influenced basalts from
322 the GSC, we estimate that the peridotitic and enriched (pyroxenitic) components in the mantle
323 source region of the GSC basalts have H₂O/La ratios of ~750 and ~350-400, respectively (Fig. 2).
324 These estimates are supported by the results of our mantle melting models (see Supplementary File)
325 utilising recent experimentally-determined mineral-melt partitioning data for H₂O (Fig. 2; Rosenthal
326 et al. 2015).

327 Unlike H₂O/La, the F/Nd ratio of the GSC basalts does not display a clear relationship with indices of
328 geochemical enrichment (e.g. [La/Sm]_n; Fig 2d). The eastern GSC basalts have an average F/Nd ratio
329 of 17.6 (±7.2; including literature data), which is slightly lower than the F/Nd ratio of the western
330 GSC basalts (20.0 ±7.3; Ingle et al., 2010). Notably, there is a large variation observed in the F/Nd
331 ratios of D- and N-MORBs from the western GSC (potentially due to the poor counting statistics of
332 EPMA analyses at low F concentrations; Ingle et al., 2010), with many of these basalts extending to
333 substantially higher F/Nd ratios than that observed in submarine basaltic glasses and naturally
334 quenched melt inclusions from the Galápagos Archipelago (Fig. 2d; Koleszar et al., 2009; Peterson et
335 al., 2017). Our new analyses for the eastern GSC basalts, however, reveal very similar F/Nd ratios to
336 those analysed from the Galápagos Platform (Fig. 2d; Peterson et al., 2017).

337 To convert the H₂O/La and F/Nd ratios of the GSC basalts into mantle source volatile concentrations
338 knowledge of the trace element compositions of the different mantle components that contribute to
339 the GSC basalts are required. In the modelling shown in Section 6, it is clear that the depleted
340 composition (i.e. low [La/Sm]_n ratios) of the plume-influenced D-MORBs from the eastern GSC can be

This represents a post-print of a peer-reviewed manuscript that has been accepted for publication in *Geochemistry, Geophysics, Geosystems* (acceptance date 19/10/2021).

341 reproduced by melting of a peridotitic component with the trace element composition of the
342 depleted DMM (Depleted MORB Mantle; Workman and Hart, 2005). Therefore, if we assume that
343 the La concentration of the depleted peridotite component beneath the eastern GSC is ~ 0.134 ppm
344 (Workman and Hart, 2005), and that this component is characterised by a H_2O/La ratio of ~ 750
345 (characteristic of the most-depleted plume-influenced GSC basalts), its H_2O concentration can be
346 calculated to be ~ 100 ppm. Very similar estimates for the H_2O content of this component are
347 obtained if H_2O/Ce is used in place of H_2O/La (~ 105 ppm H_2O ; see Supplementary Information). Our
348 estimate for the H_2O content of the depleted peridotitic component beneath the GSC is slightly
349 lower than the H_2O content estimated by Gibson and Richards (2018; 150 ppm) and similar to the
350 estimates of Michael (1988); Saal et al. (2002); Salters and Stracke (2004); and Shimizu et al.
351 (2016,2019) for the depleted MORB source mantle.

352 The Pb-isotope compositions of basalts from the western GSC imply that they contain a small melt
353 contribution from the enriched Wolf-Darwin Galápagos mantle plume component (Gibson et al.,
354 2015; Ingle et al., 2010). The H_2O content of the peridotitic mantle source beneath the western GSC,
355 however, remains uncertain owing to the lack of constraints on the trace element composition of
356 the Wolf-Darwin component. Nevertheless, in the modelling shown below, we find that the trace
357 element composition of N-MORBs located near the margin of plume influence along the western
358 GSC, which are more enriched than basalts found at similar plume-ridge distances on the eastern
359 GSC, can be produced by melting of moderately enriched mantle peridotite. We calculated this as a
360 90:10 mixture of the depleted DMM (Workman and Hart, 2005) and the enriched mantle component
361 proposed by of Donnelly et al. (2004). Using this source composition, with a La content of 0.194, we
362 estimate the H_2O content of the peridotitic mantle source beneath the western GSC is ~ 145 ppm
363 ($H_2O/La \sim 750$). Importantly, models of mantle melting involving this hypothesised peridotitic
364 component can reproduce both the trace element and H_2O contents of the western GSC N-MORBs
365 located near $95.5^\circ W$ (Fig. 2; Fig. 4).

This represents a post-print of a peer-reviewed manuscript that has been accepted for publication in *Geochemistry, Geophysics, Geosystems* (acceptance date 19/10/2021).

366 Large uncertainties in the composition of recycled oceanic crust, and the relative contribution of
367 ambient mantle peridotite and melts of a recycled crustal component to the formation of secondary
368 pyroxenites, mean that the trace element and H₂O content of a pyroxenitic component are difficult
369 to constrain. In our mantle melting models, we tested various potential solutions for the trace
370 element composition of the pyroxenitic source that might contribute to the GSC basalts, and
371 determined that a trace element composition similar to that proposed for the KG1 pyroxenite by
372 Lambart (2017) can recreate the trace element systematics of the GSC basalts (Ce, and Nd contents
373 decreased by ~10% from the Lambart, 2017 estimate; Fig. 4 & 5). Our estimated pyroxenitic source
374 composition has a La content of ~1.415 ppm that, alongside an estimated H₂O/La ratio of ~350-400
375 for this source component, provides a H₂O estimate of 495 – 565 ppm. Our new data confirms that
376 in the Galápagos mantle plume the enriched (pyroxenitic) component has a higher H₂O content than
377 the isotopically-depleted component (~100 ppm).

378 Our new estimates for the H₂O contents of the GSC peridotitic components are uninfluenced by the
379 choice of ratio to describe the behaviour of H₂O (i.e., H₂O/La or H₂O/Ce). However, the H₂O
380 estimates derived from the enriched (pyroxenite) component are higher if we use the ratio H₂O/Ce
381 (3.81 ppm Ce, H₂O/Ce ~ 170 and, therefore, H₂O ~650 ppm) rather than H₂O/La (H₂O ~495 – 565
382 ppm). However, we note that both the H₂O/La and H₂O/Ce contents of the GSC can be recreated by
383 our mantle melting models when the pyroxenitic source component has a H₂O content around ~550
384 ppm (Fig. 2c; Supplementary Information).

385 If we assume that F acts comparably to Nd during mantle melting (which is consistent with some
386 experimental data and the strong correlation between these elements in many MORB suites; Dalou
387 et al. 2012; Kendrick et al. 2017), then the F content of the depleted mantle component beneath the
388 eastern GSC can be estimated from its Nd content (assumed to be ~0.48 ppm, equivalent to that of
389 the depleted DMM; Workman and Hart, 2005) and the F/Nd of the depleted eastern GSC basalts
390 (~16 – 18). The results of these calculations give a F content of 7.7 – 8.7 ppm, the upper limit of

This represents a post-print of a peer-reviewed manuscript that has been accepted for publication in *Geochemistry, Geophysics, Geosystems* (acceptance date 19/10/2021).

391 which is shown to recreate the F/Nd systematics of the eastern GSC basalts in our forward models of
392 mantle melting (Fig. 2d).

393 Similarly, taking a source Nd concentration of ~ 0.56 ppm (calculated assuming a 90:10 mixture of
394 depleted DMM and enriched mantle for the western GSC peridotite), we can constrain the F content
395 of the peridotitic component beneath the western GSC to 8.4 – 15.6 ppm (assuming a characteristic
396 F/Nd ratio of 15-30), consistent with the western GSC data (Ingle et al., 2010). Finally, if we take the
397 F/Nd ratio of the most enriched GSC basalts (20 – 21.5) to be characteristic of the pyroxenitic mantle
398 source component, the source F concentration is calculated to be 80 – 86 ppm (source Nd
399 concentration of 4.00 ppm). However, our new mantle melting models that incorporate
400 experimental constraints on F partitioning during mantle melting (Dalou et al., 2012) reveal that a
401 pyroxenitic source F concentration >80 ppm overestimates the F/Nd ratio of the most enriched GSC
402 basalts (owing to the slightly less compatible nature of F relative to Nd during melting of a
403 pyroxenitic lithology; Fig. 2d; Supplementary Information). To provide more robust constraints on
404 the F content of the pyroxenitic mantle source, we iteratively adjusted the concentration of F in our
405 mantle melting models until the model predictions (generated by varying the proportion of plume-
406 derived channelised melt to the GSC; see Section 6) matched the GSC data. The results indicate that
407 our new data is best matched when the pyroxenitic F content is set at ~ 70 ppm.

408 6 NUMERICAL MODELS OF GALÁPAGOS PLUME-RIDGE INTERACTION

409 6.1 SIMULATING MANTLE MELTING

410 Early models of plume-ridge interaction related compositional variations in plume-influenced
411 MORBs to chemical heterogeneity on the scale of 10s to 100s of km in the sub-ridge mantle (i.e.
412 erupted magma compositions are directly related to the bulk composition of the underlying mantle;
413 Schilling, 1991; Schilling et al., 2003, 1982; Verma and Schilling, 1982). Such models suggested that

This represents a post-print of a peer-reviewed manuscript that has been accepted for publication in *Geochemistry, Geophysics, Geosystems* (acceptance date 19/10/2021).

414 isotopically and incompatible trace element enriched plume material flows towards, and then along,
415 the ridge axis where it becomes progressively diluted by mixing with ambient asthenosphere.

416 These early models recreated some of the geochemical features that are observed along plume-
417 influenced ridges; however, dynamical models of plume-ridge interaction predict no significant solid-
418 state mixing between plume and ambient mantle (Farnetani and Richards, 1995; Ito et al., 2003,
419 1997). For this reason, more recent studies of plume-ridge interaction have focused on a second
420 class of model, where mantle heterogeneity is important on length-scales of ~ 1 km or less (Ingle et
421 al., 2010; Ito and Mahoney, 2005). In this type of model, the solid sub-ridge mantle is composed of a
422 near constant mixture of enriched, hydrous peridotite or pyroxenite 'blebs' in a depleted
423 (anhydrous) peridotite matrix. Owing to their different volatile contents and/or lithological
424 properties, the enriched blebs undergo melting at greater depths than the surrounding anhydrous
425 peridotite (Ingle et al., 2010; Ito and Mahoney, 2005). Previous studies that have applied these
426 models to the GSC have concluded that variations in basalt chemistry and crustal thickness are due
427 to intermediate scale variations in mantle flow and/or melt extraction from the underlying mantle
428 (Ingle et al., 2010; Ito and Bianco, 2014; Ito and Mahoney, 2005; Shorttle et al., 2010).

429 To test the plausibility of a mixed lithology mantle in Galápagos plume-ridge interaction, we use the
430 pymelt module of Matthews et al. (2020), which simulates melting of peridotite and silica-deficient
431 pyroxenite (KG1). We build on this model by calculating the trace element composition of basaltic
432 melts formed beneath the ridge axis (see Supplementary Information) and include calculations that
433 account for the contribution of channelized melts formed by melting of a pyroxene-rich mantle
434 component in the Galápagos plume stem. By simulating the melting of a mixed lithology mantle, our
435 models differ from those of previous studies that have considered only volatile-bearing peridotite
436 source components (Gibson and Richards, 2018; Ingle et al., 2010).

437 Our new models allow us to test the influence of plume-driven active upwelling; the depth at which
438 melting ceases; and the contribution of channelised, plume-derived melts on the crustal thickness of

This represents a post-print of a peer-reviewed manuscript that has been accepted for publication in *Geochemistry, Geophysics, Geosystems* (acceptance date 19/10/2021).

439 the ridge and the trace element chemistry of the GSC basalts (see Supplementary Information for
440 full model details). To do so, we calculate the hypothetical composition of magmas produced at
441 ~0.05° intervals along the GSC, with variations in key mantle parameters (such as T_p ; U_r – the relative
442 horizontal velocity of mantle material exiting the melting region (Ingle et al., 2010; Ito and Mahoney,
443 2005); and the contribution of channelised plume-derived melts) tested to determine the dominant
444 mechanism of plume-ridge interaction in the Galápagos. Notably, the value of U_r in all models shown
445 here is depth dependent, following the relationship between U_r and pressure outlined by Ingle et al.
446 (2010). Specifically, at pressures less than that of the anhydrous peridotite solidus U_r is set to 1, but
447 at greater pressures this value is defined by the equation (derived from the work of Ito and
448 Mahoney, 2005):

$$449 \quad U_r(z) = 1 + 2 * \left(\frac{z}{H}\right) - \left(\frac{z}{H}\right)^2$$

450 where z represents the depth below the anhydrous peridotite solidus and H is the depth interval
451 that separates the initiation of mantle melting from the anhydrous peridotite solidus (see
452 supplementary information). U_{r-max} is used in this study to define the maximum value of U_r beneath
453 each area of the GSC (i.e., at the base of the melting region).

454 Here, we examine the extent to which the long and short length-scale geochemical and geophysical
455 features of plume-ridge interaction on the GSC can be recreated if we assume only solid-state flow
456 between the Galápagos mantle plume and GSC, as proposed by Ingle et al. (2010), Shorttle et al.
457 (2010) and Ito and Bianco (2014). We then highlight areas where solid-state plume-ridge interaction
458 models poorly match the available data, and examine whether additional transport of volatile-rich
459 melts in long-lived melt channels (Gibson and Richards, 2018) can account for these discrepancies.
460 The initial non-volatile trace element composition of the various mantle components beneath the
461 GSC are set as the depleted DMM (Workman and Hart, 2005), a 90:10 mixture between the depleted
462 DMM and an enriched mantle component (Donnelly et al., 2004), and an estimate for the trace

463 element composition of a silica-deficient pyroxenite (based on the composition of the KG1
464 pyroxenite presented by Lambart, 2017) for the eastern GSC peridotite component, the western GSC
465 peridotite component, and the enriched pyroxenitic component, respectively. In all of our models,
466 the trace element partition coefficients were taken from Gibson and Geist (2010) and mineral-melt
467 partition coefficients for H₂O and F were taken from recent experimental data (Dalou et al., 2012;
468 Rosenthal et al., 2015).

469 We recognise that melting parameterisations for silica-deficient pyroxenite in pymelt do not
470 consider the effects of volatiles on the pyroxenite solidus. Analyses of natural samples of mantle
471 pyroxenites have, however, shown that they have a greater capacity to host volatiles than
472 peridotites (Gibson et al., 2020). The influence of elevated H₂O contents on the pyroxenitic solidus
473 remains uncertain, although some experimental data indicates that the depression in the solidus
474 temperature caused by the presence of H₂O in a pyroxenitic mantle source is less than that seen in
475 peridotitic source components (Sorbadere et al., 2013). Nevertheless, more experimental work is
476 required to accurately parameterise the effects of H₂O on pyroxenite melting, as has been done for
477 peridotites (Katz et al., 2003). In our forward models of fractional melting we have used a H₂O
478 estimate of 550 ppm for the pyroxenite source, as this reproduces the volatile vs trace element
479 systematics of the GSC basalts (see Section 5). We accept, however, that because of uncertainties in
480 the depth of melting of volatile-bearing pyroxenite this is a non-unique solution.

481

482 **6.2 ALONG-RIDGE VARIATIONS IN GSC BASALT GEOCHEMISTRY AND CRUSTAL THICKNESS** 483 **PREDICTED BY SOLID-STATE FLOW**

484 In the models of solid-state plume-ridge interaction shown below, it is assumed that variations in
485 basalt chemistry and crustal thickness along the GSC are related to changes in the rate of mantle
486 flow below the anhydrous peridotite solidus and/or variations in source ratios (Cushman et al., 2004;
487 Gibson and Richards, 2018; Ingle et al., 2010; Ito and Bianco, 2014; Maclennan et al., 2001; Shorttle

This represents a post-print of a peer-reviewed manuscript that has been accepted for publication in *Geochemistry, Geophysics, Geosystems* (acceptance date 19/10/2021).

488 et al., 2010). Variations in mantle upwelling velocity below the anhydrous peridotite solidus are
489 hypothesized to occur as a result of the excess buoyancy flux of mantle plumes and the rapid
490 increase in mantle viscosity associated with olivine dehydration following the onset of mantle
491 melting (Hirth and Kohlstedt, 2003, 1996). In addition, although dynamical models of plume-ridge
492 interaction indicate that that there will be limited mixing between plume material and the
493 surrounding ambient mantle in the asthenosphere (Ito et al., 1997), variations in source proportions
494 beneath the GSC are considered owing to the clear spatial heterogeneity in the composition of the
495 Galápagos mantle plume (Gleeson et al., 2021; Harpp and Weis, 2020; Harpp and White, 2001;
496 White et al., 1993).

497 In the following solid-state plume-ridge interaction models, the relative rate at which mantle
498 material exits the melting region at the base of the melt column (U_{r-max} ; horizontal velocity relative to
499 a scenario where no active upwelling is present) is assumed to decrease with increasing distance
500 from the GTF (Table 1). This relationship (between U_{r-max} and longitude) is selected following the
501 study of Ingle et al. (2010) and qualitatively follows the change in mantle flow velocities predicted by
502 the numerical models of Bianco et al., (2013) and Ito and Bianco (2014). Similarly, we test various
503 relationships between longitude and the mantle potential temperature (T_p), the mass fraction of
504 pyroxenitic material in the source and the pressure at the base of the lithosphere/top of the melt
505 column.

506 We iteratively adjusted these parameters until our models produced a satisfactory match to both
507 the composition of the GSC basalts and the crustal thickness estimates of Canales et al. (2002) and
508 Mittelstaedt et al. (2014). Example model results are shown in Figure 4 and Table 1 and indicate that
509 solid-state plume-ridge interaction produces an excellent match to the composition of most basalts
510 erupted west of 86°W on the eastern GSC, and the D-MORBs and N-MORBs located on the western
511 GSC. In addition, the model results reveal clear differences between the eastern and western GSC.
512 For example, to generate the greater crustal thickness of the oceanic crust produced along the

This represents a post-print of a peer-reviewed manuscript that has been accepted for publication in *Geochemistry, Geophysics, Geosystems* (acceptance date 19/10/2021).

513 eastern GSC (Mittelstaedt et al., 2014), our models indicate that the mantle potential temperature
514 beneath the eastern GSC adjacent to the GTF is ~ 5 °C higher than at any point beneath the western
515 GSC. The change in crustal thickness along each ridge segment (i.e., the eastern and western GSC) is
516 driven by a combination of changes in mantle potential temperature (~ 10 °C), the proportion of
517 pyroxenite in the mantle source and contribution of plume-driven upwelling in regions closest to the
518 GTF. Additionally, our results indicate that the pressure at the top of the melting region is greater in
519 regions adjacent to the GTF, possibly owing to conductive cooling effects of the cold lithospheric
520 material of the transform fault (Le Voyer et al., 2015) and the increased proportion of pyroxenite in
521 the mantle source (Brunelli et al., 2018). This increase in the pressure of melt termination is required
522 to avoid a 'run-away' increase in the crustal thickness of the ridge in regions where the contribution
523 of active plume driven upwelling is greatest.

524 Figure 4 also highlights several pitfalls that are associated with solid-state plume-ridge interaction
525 models that account for lateral variations in mantle flow. For example, modelled crustal thickness
526 increases systematically along the western GSC towards the GTF, which is qualitatively consistent
527 with the crustal thickness variations predicted in numerical simulations of mantle flow for on-axis (or
528 near-axis) mantle plumes (e.g. Iceland; Bianco et al., 2013). Recent studies have, however, shown
529 that there are three ~ 20 km wide regions between $\sim 92.5^\circ\text{W}$ and the GTF with crustal thickness
530 anomalies of ~ 1 km (Mittelstaedt et al., 2014), which our simple model of solid-state plume-ridge
531 interaction cannot capture (Fig. 4). In addition, although the solid-state plume-ridge interaction
532 model shown in Fig. 4 accurately recreates the chemistry of the western GSC N-MORBs located west
533 of 92.5°W and east of 91.8°W , they are not able to recreate the composition of the more enriched
534 basalts located between 92.5°W to 91.8°W , or the composition of anomalously enriched basalts that
535 are present between 89.5 and 92°W on the GSC.

536 Some of these discrepancies may be addressed if we consider non-symmetric spreading of solid
537 plume material. One possible mechanism that might facilitate such flow is thermal erosion of a sub-

This represents a post-print of a peer-reviewed manuscript that has been accepted for publication in *Geochemistry, Geophysics, Geosystems* (acceptance date 19/10/2021).

538 lithospheric channel between the mantle plume and adjacent ridge (Kingsley and Schilling, 1998;
539 Schilling, 1991). However, geophysical and petrological estimates indicate that there are no areas of
540 significant (i.e. >10 km) lithospheric thinning beneath the volcanic lineaments connecting the
541 western GSC to the Galápagos Archipelago (Gibson and Geist, 2010; Harpp et al., 2014c). Therefore,
542 any thermal erosion of the lithosphere beneath the northern Galapagos is unlikely to be sufficient to
543 trap plume material and influence plume outflow (cf. Gibson et al., 2015). In addition, some of the
544 offsets between our model predictions and the GSC data may result from the use of a 2D model
545 scenario to describe a 3D system. In particular, the influence of transform faults on upper mantle
546 dynamics is not considered here, but could influence the composition of basalts erupted close to
547 these structures (Weatherley and Katz, 2010), and the eastward motion of the Nazca plate above the
548 Galápagos plume stem is likely to cause some deflection of solid plume material in the upper mantle
549 (e.g. Harpp and White, 2001). Nevertheless, we believe that these factors are unlikely to account for
550 the shortcomings of the solid-state plume ridge interaction models.

551 **6.3 CHANNELISED FLOW OF H₂O-RICH MELTS TO THE GSC**

552 Numerical models of mantle melting beneath oceanic spreading centres have shown that highly
553 permeable melt channels are a natural consequence of melting during upwelling of a heterogeneous
554 mantle (Katz and Weatherley, 2012; Weatherley and Katz, 2012). As chemical interaction of
555 channelised melts with the surrounding mantle is expected to be limited (Weatherley and Katz,
556 2012), channelised melt flow might represent an efficient method of transporting geochemically
557 enriched material to nearby spreading centres. In addition, highly-permeable melt channels have
558 been shown to be thermodynamically stable over distances up to ~1500 km (for channels ~50 – 60m
559 in radius) and the transport timescales of volatile-rich melts in these channels are significantly lower
560 than the timescales required by U-series disequilibria (Kokfelt et al., 2005; Mittal and Richards,
561 2017). Therefore, conceptual models involving the delivery of plume-derived compositionally-
562 enriched melts to MORs in highly permeable melt channels have been proposed for the Galápagos
563 and other sites of plume-ridge interaction worldwide (Gibson et al., 2015; Gibson and Richards,

This represents a post-print of a peer-reviewed manuscript that has been accepted for publication in *Geochemistry, Geophysics, Geosystems* (acceptance date 19/10/2021).

564 2018; Mittal and Richards, 2017). In these models, the primary factor driving the migration of melts
565 from the stem of the upwelling plume (>60 – 80 km depth) to the sub-ridge mantle (<40-60 km
566 depth) is melt buoyancy. Melt channelisation was likely initiated when the Galápagos plume was on-
567 axis (at >5 Ma) and has been maintained during ridge migration away from the plume stem (Gibson
568 et al. 2015).

569 6.3.1 Variations in the supply of channelized melts to the western and eastern GSC

570 The solid-state plume-ridge interaction models described in Section 6.2 require relative horizontal
571 flow velocities at the base of the melting region (U_{r-max}) of ~6-8 to explain the geochemical and
572 geophysical signatures of plume-ridge interaction between 90.5°W and 90.8°W (Fig. 4). Values of U_{r-}
573 max up to ~15 have previously been suggested for the GSC, based on the buoyancy flux of the
574 Galápagos mantle plume (Ingle et al., 2010; Sleep, 1990).

575 In the following models, however, we assume that: (i) the change in the relative mantle flow velocity
576 below the anhydrous peridotite solidus is small ($U_{r-max} < 1.5 - 2.5$); and (ii) variations in the
577 geochemical and geophysical signatures of plume-ridge interaction along the GSC are instead
578 derived from slight changes in T_p and/or the supply of channelised melts from the Galápagos plume
579 stem (Table 1). The volatile and non-volatile trace element composition of the channelised melts are
580 calculated as the non-modal aggregated fractional melt of the enriched (pyroxenitic) mantle
581 component (see Supplementary Information for detailed methods). We assume that the melt
582 channels form at depths below the anhydrous peridotite solidus (>2.5 - 3 GPa at $T_p = 1400^\circ\text{C}$) and
583 various values for the pressure of channel initiation/formation were tested.

584 The crustal thickness and geochemical characteristics of the eastern GSC are generally well-matched
585 by our solid-state models of plume-ridge interaction. Nevertheless, we recognise that this is not a
586 unique solution as these observations can also be reproduced if we model an exponential decrease
587 in the proportion of channelized melts supplied to the eastern GSC with increasing distance to the
588 centre of plume upwelling (Fig. 5). In this model, the decrease in the supply of channelized, enriched

This represents a post-print of a peer-reviewed manuscript that has been accepted for publication in *Geochemistry, Geophysics, Geosystems* (acceptance date 19/10/2021).

589 melt to the eastern GSC with increasing distance to the Galapagos plume may be related to a decline
590 in the number of melt channels that remain thermodynamically stable over the increased plume-ride
591 distance (Mittal and Richards, 2017), or changes in the angle at which melt channels intersect the
592 ridge axis (i.e. assuming the melt channels initiate from a single location beneath the Galápagos
593 Archipelago, the melt channels may be orientated roughly perpendicular to the ridge axis near the
594 GTF but this orientation is not maintained further east; Fig. 6). This hypothesis shares many
595 similarities to the model proposed for solid-state plume-ridge interaction by Shorttle et al. (2010),
596 but has the advantage of being able to simultaneously explain the enriched geochemical signatures
597 along the GSC and the depleted isotopic compositions of the island of Marchena and Genovesa in
598 the Northern Galápagos Volcanic Province (Gibson et al., 2015; Harpp et al., 2014c).

599 At the closest point to the Galápagos Archipelago, the eastern GSC is located only ~100-150 km
600 north of the centre of plume upwelling, identified at 100 km depth in the seismic tomography study
601 of Villagomez et al. (2014). In their theoretical study, Mittal and Richards (2017) showed that over
602 such short plume-ridge separation distances, melt channels ~5 m in radius are likely to be
603 thermodynamically stable (assuming a constant heat flux source). This channel radius is within the
604 range observed in dunitic/melt channels observed in ophiolites worldwide (e.g., dunitic channels in
605 the Oman ophiolite can reach 200 m across; Kelemen et al., 1997). We suggest, therefore, that the
606 delivery of compositionally-enriched melts to the eastern GSC in highly permeable melt channels
607 only a few metres in thickness could generate the geochemical enrichment observed along the
608 eastern GSC.. The continued presence of channelised melts along the whole of the eastern GSC,
609 even if only in very small proportions (<1%), maintains the possibility that anomalously enriched
610 basalts can be observed at the surface at plume-ridge interaction distances in excess of 300 – 400
611 km (see Section 6.3.2). However, while the geochemical and geophysical features observed on the
612 eastern GSC can be produced by both solid-state and melt transport models of plume ridge
613 interaction, many of the discrepancies between the GSC data and solid-state models of plume-ridge

614 interaction occur on the western GSC (e.g. the composition of basalts located between 92.5°W and
615 91.8 °W).

616 Our models reveal that the geochemical and geophysical signatures of plume-ridge interaction on
617 the western GSC cannot be produced by a similar model to that used to recreate the eastern GSC
618 data (i.e. a gradually decreasing supply of channelised melts with increasing plume-ridge distance).
619 Instead, we find that the discrepancies between the western GSC geochemical and geophysical data
620 and our solid-state plume-ridge interaction models can be overcome by simulating a low level of
621 channelised melt contribution to the western GSC between ~93°W and the GTF (<10% channelised
622 melt contribution) and focused delivery of additional channelized melts to the western GSC beneath
623 each of the three volcanic lineaments in the northern Galápagos (Fig. 5), as proposed by Mittal and
624 Richards (2017) and Gibson and Richards (2018). In the model used here, the proportion of
625 channelized melt supplied to the western GSC beneath each of the lineaments is assumed to follow
626 3 overlapping normal distributions, where the greatest rate of supply occurs at the intersection of
627 each of the three volcanic lineaments with the GSC (92.25°W, 91.8°W, 91.3°W). The results provide
628 an excellent match to the geochemical data (including volatiles) from the western GSC and
629 reproduce the short length-scale variations in crustal thickness observed at the intersection of each
630 volcanic lineament with the western GSC (Fig. 5; Mittelstaedt et al., 2014). It is important to note,
631 however, that the compositional variability between the different seamounts and islands that make
632 up the three volcanic lineaments indicates that their magmatic systems are locally complex (Harpp
633 et al., 2014c).

634 Notably, the models used to recreate the geochemical and geophysical signatures of plume-ridge
635 interaction along the western and eastern sections of the GSC are very different, although similar
636 levels of geochemical enrichment are observed on both ridge segments. We propose that the
637 differences may arise from the greater plume-ridge distance of the western GSC compared to the
638 eastern GSC (~100 km greater). Specifically, we suggest that the large plume-ridge interaction

639 distance of the western GSC results in the amalgamation of several melt channels into a focused
640 region beneath each volcanic lineament (and thus localised delivery of channelised melt to the ridge
641 axis). This coalescence may help to maintain the thermodynamic stability of the melt channels over
642 the greater plume-ridge distance (Fig. 6; Mittal and Richards, 2017), and is consistent with the
643 amalgamation of high porosity (channelised) regions observed in numerical models of mantle
644 melting (e.g. Katz and Weatherley, 2012). Nevertheless, the coincidence of a ~10 km wide crustal
645 thickness anomaly (Mittelstaedt et al., 2014) and two anomalously volatile-rich samples (TR164 6D-
646 1g and 2g, which lie outside the compositions predicted by our along-ridge models; Fig. 5) on the
647 eastern GSC at 89.59°W indicate that localised variations in the volume of melt delivered to the
648 eastern GSC exist. In addition, the sample density along the eastern GSC is lower than that along the
649 western GSC, which raises the possibility that other short length-scale geochemical heterogeneities
650 may be present in the region between 89.59°W and 90.8°W, but are unsampled. As such, more data
651 is required to confirm that differences in the characteristics of melt channelisation to the western
652 and eastern GSC control the geochemical and geophysical features of plume-ridge interaction in the
653 Galápagos.

654 6.3.2 Anomalously enriched GSC basalts

655 The above models of plume-ridge interaction via channelised transport of volatile-rich melts
656 accurately recreate the broad-scale, and some of the short length-scale, geochemical and
657 geophysical features of plume influence on the GSC. There are, however, a series of basalts located
658 along plume-influenced segments of the GSC (and in other regions of plume-ridge interaction
659 worldwide) that display compositions which are too enriched to be explained by any of the models
660 outlined above (e.g. TR164 6d-1g at 89.59 °W; Gibson and Richards, 2018). These anomalously
661 enriched basalts, which typically contain $[H_2O]_{(8)}$ contents >0.4 wt%, have previously been explained
662 through the localised delivery of large volumes of channelised melt to the ridge, overwhelming the
663 contribution of more depleted melts formed in the shallow mantle (Gibson and Richards, 2018;

This represents a post-print of a peer-reviewed manuscript that has been accepted for publication in *Geochemistry, Geophysics, Geosystems* (acceptance date 19/10/2021).

664 Mittal and Richards, 2017). To build on this previous work, we compared the results of our mantle
665 melting models that incorporate the presence of channelised, plume-derived melts to the
666 composition of the anomalously enriched basalts located along the GSC.

667 In detail, we calculated the Root Mean Squared Error (RMSE) between our mantle melting models
668 and each of the anomalously enriched GSC basalts. The mantle potential temperature of the
669 Galápagos plume (where the channelised melts are being formed) is set at 1400 °C in all calculations,
670 and we tested variations in the contribution of channelised melt (0 – 50%), and the pressure of
671 channel formation (2.8 - 3.6 GPa). This pressure range was chosen as initial models showing the
672 influence of incorporating plume-derived channelised melts demonstrated that channel formation at
673 lower pressures is unable to recreate the high $[La/Sm]_n$ ratio of the anomalously enriched GSC
674 basalts (Fig. 7a). The proportion of pyroxenite in the Galapagos plume stem was set at ~20%
675 (Gleeson et al., 2021).

676 The model calculations demonstrate that the anomalously enriched basalts from the GSC, which
677 have $[H_2O]_{(8)}$ contents >0.4 wt%, likely contain a >15% contribution of channelised, plume-derived
678 melts (Fig. 7). However, the large proportion of channelised melt required to recreate the
679 composition of these anomalously enriched basalts is inconsistent with the magnitude of the crustal
680 thickness anomalies found in these locations (Mittelstaedt et al., 2014). For example, at ~89.59 °W
681 on the eastern GSC, where a crustal thickness anomaly of ~0.5-1 km is observed (~9.5 km thick crust
682 compared to the model predictions of ~8.5 – 9 km), the >15% contribution of channelised melt
683 required to reproduce the geochemical signature of the highly enriched GSC basalts would, in
684 theory, generate a crustal thickness anomaly >1-1.5 km (Fig. 7). The discrepancy between the
685 predicted and observed crustal thickness is even greater at the location of sample TR164 26D-3g
686 (90.95 °W) where no crustal thickness anomaly is observed, but a >30% contribution of channelised
687 melt is required to reproduce the trace and volatile element systematics of the erupted basalt.

This represents a post-print of a peer-reviewed manuscript that has been accepted for publication in *Geochemistry, Geophysics, Geosystems* (acceptance date 19/10/2021).

688 We therefore suggest that the high proportion of channelized melt that contributes to the
689 composition of the most volatile-rich GSC basalts is a result of inefficient mixing of channelised melts
690 with more depleted magmas produced at shallower depths in the sub-ridge mantle (Fig. 8). This
691 scenario that is consistent with the proposed chemical isolation of high-pressure channelised melts
692 with the surrounding mantle peridotite during magma transport (Katz and Weatherley, 2012; Keller
693 and Katz, 2016). In this scenario, volatile-rich basaltic magmas may reach the surface even in regions
694 where there is a relatively low flux of channelized plume-derived melts to the GSC (Fig. 8). In fact,
695 the low melt flux at large plume-ridge interaction distances (e.g. sample ST7 17D-1g; 86.13 °W), and
696 locations that are proximal to large transform faults (e.g. samples TR164 26D-3g; 90.95 °W,
697 respectively), might restrict the formation of a steady-state magma chambers (Le Voyer et al., 2015;
698 Sinton and Detrick, 1992). As a result, it is possible that magma homogenisation is subdued at these
699 locations, increasing the probability of enriched basalts being observed at the surface (Langmuir and
700 Bender, 1984; Le Voyer et al., 2015).

701 7 QUANTIFYING THE OUTFLOW OF H₂O ON PLUME-INFLUENCED SECTIONS 702 OF THE GALÁPAGOS SPREADING CENTRE

703 Our new volatile data expand the small number of analyses previously published for the eastern GSC
704 (e.g. Byers et al., 1983), and extend the existing GSC database of volatile element analyses to cover
705 the entire region of plume-influenced ridge. Nevertheless, for many basalts erupted along plume-
706 influenced sections of the GSC, volatile data are absent and we thus use the available fractional
707 crystallisation corrected H₂O data from both the eastern and western GSC to identify a non-volatile
708 trace element proxy that can be used to estimate the H₂O contents of the remaining GSC basalts.

709 The $[H_2O]_{(8)}$ (that is, the water concentration of each sample once it has been fractional
710 crystallisation corrected to 8 wt% MgO) and $[Sm/Yb]_n$ contents of basalts from both the western and

This represents a post-print of a peer-reviewed manuscript that has been accepted for publication in *Geochemistry, Geophysics, Geosystems* (acceptance date 19/10/2021).

711 eastern GSC display a positive correlation ($r^2=0.907$; Fig 3a). As such, we use the $[Sm/Yb]_n$ ratio of the
712 GSC basalts as a proxy for their fractionation corrected H_2O contents ($[H_2O]_{(8)}$). $[Sm/Yb]_n$ is chosen
713 rather than $[Ce/Yb]_n$, as suggested by Gibson and Richards (2018), because our new data shows a
714 small number of highly-enriched basalts from the western GSC have slightly higher $[H_2O]_{(8)}$ at a given
715 $[Ce/Yb]_n$ than the other GSC basalts (Fig. 3b). As a result, the correlation between $[H_2O]_{(8)}$ and
716 $[Ce/Yb]_n$ is subtly different for basalts from the eastern and western GSC (gradients of 0.142 and
717 0.162, respectively; Fig. 3b).

718 Taking our new volatile data from the eastern GSC, together with published volatile data from the
719 western GSC (Cushman et al., 2004; Ingle et al., 2010), and estimated volatile contents based on the
720 trace element content of additional GSC basalts (Christie et al., 2005), we can use our 2 component
721 models of plume-ridge interaction to calculate the outflux of H_2O from plume-influenced sections of
722 the GSC. This is achieved using our along-ridge mantle melting models that incorporate the influence
723 of channelised melt transport and accurately recreate the trace element composition and crustal
724 thickness of the plume-influenced GSC, alongside the following equation:

$$725 \quad H_2O^{flux} (kg/(m. yr)) = (C_{H_2O}^{mix} (ppm) \times 10^{-6}) \times SR (m/yr) \times CT (m) \times 2900 (kg/m^3)$$

726 Where $C_{H_2O}^{mix}$ is the H_2O concentration of the fully homogenized primary mantle melts and CT is the
727 crustal thickness produced at each calculation interval along the GSC (calculation step size of $\sim 0.05^\circ$).
728 SR represents the spreading rate of the GSC (Schilling et al., 2003), and the density of the melt phase
729 is assumed to be $\sim 2900 \text{ kg/m}^3$.

730 Our results indicate that incorporation of enriched material from the Galápagos mantle plume
731 causes the flux of H_2O to increase by a factor of 3 from $86^\circ W$ to $90.8^\circ W$ on the eastern GSC (Fig. 9).
732 On the western GSC, the flux of H_2O is greatest in regions where the volcanic lineaments intersect
733 the GSC, and the maximum flux of H_2O from any part of the western GSC is similar to the maximum
734 H_2O flux along the eastern GSC ($\sim 4000 \text{ kg.m}^{-1}.\text{yr}^{-1}$; Fig. 9). In addition, our calculations show that
735 volatile-rich channelized melts contribute up to $\sim 60\%$ of the H_2O and F outflux, from localised

This represents a post-print of a peer-reviewed manuscript that has been accepted for publication in *Geochemistry, Geophysics, Geosystems* (acceptance date 19/10/2021).

736 regions of the plume-influenced GSC (Fig. 9; Supplementary Information). Overall, melt
737 channelisation may account for ~35% of the H₂O outflux from the western GSC between 90.8°W and
738 92.5°W and ~25% of the H₂O outflux between 86°W and 90.8°W on the eastern GSC.

739 While transport of volatile-rich melts to the GSC has a clear influence on the H₂O and F
740 concentrations of the erupted magmas, little to no variations are seen in the ³He/⁴He ratio of these
741 basalts (Graham et al., 2014). This observation requires that melts reaching the GSC have much
742 lower ³He/⁴He than those forming deep in the plume beneath the western Galápagos Archipelago.
743 The lack of a primordial ³He/⁴He signature in plume-influenced GSC basalts may be because: (i) rapid
744 vertical transport of high-pressure melts with elevated ³He/⁴He ratios is restricted to the vicinity of
745 the plume stem (Kurz and Geist, 1999; Villagómez et al. 2014; Peterson et al. 2017); or (ii) the ‘deep’
746 plume-stem melts that are being transported laterally to the ridge via channelised flow may be
747 derived from blebs of recycled lithosphere (Gleeson et al., 2020) with similar or lower ³He/⁴He ratios
748 to MORBs (e.g. Day et al., 2015).

749 8 CONCLUSIONS

750 Our study uses new analyses of volatiles (H₂O, F, Cl, and S) in basaltic glass chips from the Galápagos
751 Spreading Centre, as well as two-component mantle melting models, to investigate the nature and
752 dynamics of plume-ridge interaction in the Galápagos. The results of this study can be summarized in
753 4 key points:

- 754 1. Solid-state transfer of plume material between the Galápagos mantle plume and adjacent
755 GSC can account for some of the long length-scale (~100 – 1000 km wide) geochemical and
756 geophysical signatures of plume-ridge interaction. However, solid-state plume-ridge
757 interaction models cannot easily explain the presence of short length-scale (<10 km)
758 geochemical and geophysical heterogeneities.

- 759 2. The long and short length-scale features of plume-ridge interaction in the Galápagos are
760 readily explained by plume-ridge interaction models that include the transport of volatile-
761 rich melts to the GSC in melt-dominated channels.
- 762 3. One key feature of plume-influenced ridge segments is the presence of anomalously
763 enriched basalts, i.e. those that are substantially more enriched with respect to their trace
764 element contents than their neighbouring basalts (e.g. Gibson and Richards, 2018). The
765 strongly enriched basalts on the GSC also have anomalously-high Fe isotope ratios that have
766 been interpreted as reflecting large contributions of melt from a pyroxenitic mantle
767 component within the Galápagos plume (Gleeson et al., 2020). While we acknowledge that
768 the role of pyroxenite is controversial, and more work needs to be done, the key findings of
769 our models for the mechanisms of plume-ridge interaction are, to a large extent,
770 independent of the source lithology chosen for the enriched mantle component in the
771 source region of the GSC basalts (i.e. peridotite vs pyroxenite).
- 772 4. Our new mantle melting models indicate that the composition of the GSC basalts are
773 controlled by the incomplete mixing of channelised, volatile-rich melts from the Galápagos
774 mantle plume with more depleted melts formed by adiabatic decompression in the sub-
775 ridge mantle. They also suggest that the most enriched basalts from the GSC may contain a
776 >40% contribution from channelized, plume-derived melt.
- 777 5. Our results indicate that plume-ridge interaction causes the H₂O flux out of the GSC to vary
778 by a factor of ~3, with the greatest amounts observed on the eastern GSC near the
779 Galápagos Transform Fault and at the intersections of volcanic lineaments with the western
780 GSC (up to ~4000 kg.m⁻¹.yr⁻¹). We suggest that delivery of volatile-rich channelised melts to
781 the ridge axis might account for up to ~60% of the H₂O flux out of these regions.

782 ACKNOWLEDGEMENTS

783 M.L.M.G. was supported by a NERC (Natural Environmental Research Council) Research Training
784 Student Grant (NE/L002507/1) and a Research Fellowship funded by the Royal Commission for the
785 Exhibition of 1851. S.A.G. was supported by grant RG57434 for research in Galápagos. We are
786 grateful to Iris Buisman and Richard Hinton for assistance with EPMA and SIMS analysis, respectively.
787 The Secondary Ion Mass Spectrometry analysis was carried out at the Edinburgh Ion Microprobe
788 Facility (award IMF622/0517). We thank Mike Stock for his help with SIMS data collection and early
789 discussions about the project. We are also grateful to Mark Richards and Tushar Mittal for sharing
790 their thoughts on plume-ridge interaction, together with Karen Harpp, Peter Michael and an
791 anonymous reviewer whose constructive comments greatly improved the quality of our manuscript.

792 DATA AND CODE AVAILABILITY

793 Data collected in this study, and the code used to analyse the data, can be found through
794 <https://zenodo.org/badge/latestdoi/379869011>

795 REFERENCES

- 796 Adam, J., Turner, M., Hauri, E.H., Turner, S., 2016. Crystal/melt partitioning of water and other
797 volatiles during the near-solidus melting of mantle peridotite: Comparisons with non-volatile
798 incompatible elements and implications for the generation of intraplate magmatism. *Am.*
799 *Mineral.* 101, 876–888. <https://doi.org/10.2138/am-2016-5437>
- 800 Asimow, P.D., Langmuir, C.H., 2003. The importance of water to oceanic mantle melting regimes.
801 *Nature* 421, 815–820. <https://doi.org/10.1038/nature01429>
- 802 Behn, M.D., Sinton, J.M., Detrick, R.S., 2004. Effect of the Galápagos hotspot on seafloor volcanism
803 along the Galápagos Spreading Center (90.9–97.6°W). *Earth Planet. Sci. Lett.* 217, 331–347.
804 [https://doi.org/10.1016/S0012-821X\(03\)00611-3](https://doi.org/10.1016/S0012-821X(03)00611-3)
- 805 Bianco, T.A., Ito, G., van Hunen, J., Mahoney, J.J., Ballmer, M.D., 2013. Geochemical variations at
806 ridge-centered hotspots caused by variable melting of a veined mantle plume. *Earth Planet.*
807 *Sci. Lett.* 371–372, 191–202. <https://doi.org/10.1016/j.epsl.2013.03.050>
- 808 Blacic, T.M., Ito, G., Canales, J.P., Detrick, R.S., Sinton, J., 2004. Constructing the crust along the
809 Galapagos Spreading Center 91.3°–95.5°W: Correlation of seismic layer 2A with axial magma
810 lens and topographic characteristics. *J. Geophys. Res. Solid Earth* 109.
811 <https://doi.org/10.1029/2004JB003066>
- 812 Braun, M.G., Sohn, R.A., 2003. Melt migration in plume–ridge systems. *Earth Planet. Sci. Lett.* 213,
813 417–430. [https://doi.org/10.1016/S0012-821X\(03\)00279-6](https://doi.org/10.1016/S0012-821X(03)00279-6)

- 814 Brunelli, D., Cipriani, A., Bonatti, E., 2018. Thermal effects of pyroxenites on mantle melting below
815 mid-ocean ridges. *Nat. Geosci.* 11, 7.
- 816 Byers, C.D., Muenow, D.W., Garcia, M.O., 1983. Volatiles in basalts and andesites from the
817 Galapagos Spreading Center, 85° to 86°W. *Geochim. Cosmochim. Acta* 47, 1551–1558.
818 [https://doi.org/10.1016/0016-7037\(83\)90181-3](https://doi.org/10.1016/0016-7037(83)90181-3)
- 819 Cabral, R.A., Jackson, M.G., Koga, K.T., Rose-Koga, E.F., Hauri, E.H., Whitehouse, M.J., Price, A.A.,
820 Day, J.M.D., Shimizu, N., Kelley, K.A., 2014. Volatile cycling of H₂O, CO₂, F, and Cl in the
821 HIMU mantle: A new window provided by melt inclusions from oceanic hot spot lavas at
822 Mangaia, Cook Islands. *Geochem. Geophys. Geosystems* 15, 4445–4467.
823 <https://doi.org/10.1002/2014GC005473>
- 824 Canales, J.P., Dunn, R.A., Ito, G., Detrick, R.S., Sallarès, V., 2014. Effect of Variations in Magma Supply
825 on the Crustal Structure of Mid-Ocean Ridges: Insights from the Western Galápagos
826 Spreading Center, in: Harpp, K.S., Mittelstaedt, E., d'Ozouville, N., Graham, D.W. (Eds.),
827 *Geophysical Monograph Series*. John Wiley & Sons, Inc, Hoboken, New Jersey, pp. 363–391.
828 <https://doi.org/10.1002/9781118852538.ch17>
- 829 Canales, J.P., Ito, G., Detrick, R.S., Sinton, J., 2002. Crustal thickness along the western Galápagos
830 Spreading Center and the compensation of the Galápagos hotspot swell. *Earth Planet. Sci.*
831 *Lett.* 203, 311–327. [https://doi.org/10.1016/S0012-821X\(02\)00843-9](https://doi.org/10.1016/S0012-821X(02)00843-9)
- 832 Christie, D.M., Werner, R., Hauff, F., Hoernle, K., Hanan, B.B., 2005. Morphological and geochemical
833 variations along the eastern Galápagos Spreading Center. *Geochem. Geophys. Geosystems*
834 6, n/a-n/a. <https://doi.org/10.1029/2004GC000714>
- 835 Cushman, B., Sinton, J., Ito, G., Eaby Dixon, J., 2004. Glass compositions, plume-ridge interaction, and
836 hydrous melting along the Galápagos Spreading Center, 90.5°W to 98°W. *Geochem.*
837 *Geophys. Geosystems* 5. <https://doi.org/10.1029/2004GC000709>
- 838 Dalou, C., Koga, K. T., Shimizu, N., 2012. Experimental determination of F and Cl partitioning
839 between lherzolite and basaltic melt. *Contrib. Mineral. Petrol.* 163, 591–609.
- 840 Danyushevsky, L.V., Eggins, S.M., Falloon, T.J., Christie, D.M., 2000. H₂O Abundance in Depleted to
841 Moderately Enriched Mid-ocean Ridge Magmas; Part I: Incompatible Behaviour, Implications
842 for Mantle Storage, and Origin of Regional Variations. *J. Petrol.* 41, 1329–1364.
843 <https://doi.org/10.1093/petrology/41.8.1329>
- 844 Day, J.M.D., Barry, P.H., Hilton, D.R., Burgess, R., Pearson, D.G., Taylor, L.A., 2015. The helium flux
845 from the continents and ubiquity of low-³He/⁴He recycled crust and lithosphere. *Geochim.*
846 *Cosmochim. Acta* 153, 116–133. <https://doi.org/10.1016/j.gca.2015.01.008>
- 847 Detrick, R.S., Sinton, J.M., Ito, G., Canales, J.P., Behn, M., Blacic, T., Cushman, B., Dixon, J.E., Graham,
848 D.W., Mahoney, J.J., 2002. Correlated geophysical, geochemical, and volcanological
849 manifestations of plume-ridge interaction along the Galápagos Spreading Center. *Geochem.*
850 *Geophys. Geosystems* 3, 1–14. <https://doi.org/10.1029/2002GC000350>
- 851 Dixon, J.E., 1997. Degassing of alkalic basalts. *Am. Mineral.* 82, 368–378.
852 <https://doi.org/10.2138/am-1997-3-415>
- 853 Dixon, J.E., Bindeman, I.N., Kingsley, R.H., Simons, K.K., Le Roux, P.J., Hajewski, T.R., Swart, P.,
854 Langmuir, C.H., Ryan, J.G., Walowski, K.J., Wada, I., Wallace, P.J., 2017. Light Stable Isotopic
855 Compositions of Enriched Mantle Sources: Resolving the Dehydration Paradox. *Geochem.*
856 *Geophys. Geosystems* 18, 3801–3839. <https://doi.org/10.1002/2016GC006743>
- 857 Donnelly, K.E., Goldstein, S.L., Langmuir, C.H., Spiegelman, M., 2004. Origin of enriched ocean ridge
858 basalts and implications for mantle dynamics. *Earth Planet. Sci. Lett.* 226, 347–366.
859 <https://doi.org/10.1016/j.epsl.2004.07.019>
- 860 Farnetani, D.G., Richards, M.A., 1995. Thermal entrainment and melting in mantle plumes. *Earth*
861 *Planet. Sci. Lett.* 136, 251–267. [https://doi.org/10.1016/0012-821X\(95\)00158-9](https://doi.org/10.1016/0012-821X(95)00158-9)
- 862 Geist, D., Naumann, T., Larson, P., 1998. Evolution of Galapagos Magmas: Mantle and Crustal
863 Fractionation without Assimilation. *J. Petrol.* 39, 953–971.
864 <https://doi.org/10.1093/etroj/39.5.953>

This represents a post-print of a peer-reviewed manuscript that has been accepted for publication in *Geochemistry, Geophysics, Geosystems* (acceptance date 19/10/2021).

- 865 Gibson, S.A., Dale, C.W., Geist, D.J., Day, J.A., Brüggmann, G., Harpp, K.S., 2016. The influence of melt
866 flux and crustal processing on Re–Os isotope systematics of ocean island basalts: Constraints
867 from Galápagos. *Earth Planet. Sci. Lett.* 449, 345–359.
868 <https://doi.org/10.1016/j.epsl.2016.05.021>
- 869 Gibson, S.A., Geist, D., 2010. Geochemical and geophysical estimates of lithospheric thickness
870 variation beneath Galápagos. *Earth Planet. Sci. Lett.* 300, 275–286.
871 <https://doi.org/10.1016/j.epsl.2010.10.002>
- 872 Gibson, S.A., Geist, D.J., Richards, M.A., 2015. Mantle plume capture, anchoring, and outflow during
873 Galápagos plume-ridge interaction: Mantle plume capture & outflow. *Geochem. Geophys.*
874 *Geosystems* 16, 1634–1655. <https://doi.org/10.1002/2015GC005723>
- 875 Gibson, S.A., Richards, M.A., 2018. Delivery of deep-sourced, volatile-rich plume material to the
876 global ridge system. *Earth Planet. Sci. Lett.* 499, 205–218.
877 <https://doi.org/10.1016/j.epsl.2018.07.028>
- 878 Gibson, S.A., Rooks, E.E., Day, J.A., Petrone, C.M., Leat, P.T., 2020. The role of sub-continental mantle
879 as both “sink” and “source” in deep Earth volatile cycles. *Geochim. Cosmochim. Acta* 275,
880 140–162. <https://doi.org/10.1016/j.gca.2020.02.018>
- 881 Gleeson, M., Soderman, C., Matthews, S., Cottaar, S., Gibson, S., 2021. Geochemical Constraints on
882 the Structure of the Earth’s Deep Mantle and the Origin of the LLSVPs. *Geochem. Geophys.*
883 *Geosystems* 22. <https://doi.org/10.1029/2021GC009932>
- 884 Gleeson, M.L.M., Gibson, S.A., 2019. Crustal controls on apparent mantle pyroxenite signals in
885 ocean-island basalts. *Geology*. <https://doi.org/10.1130/G45759.1>
- 886 Gleeson, M.L.M., Gibson, S.A., Williams, H.M., 2020. Novel insights from Fe-isotopes into the
887 lithological heterogeneity of Ocean Island Basalts and plume-influenced MORBs. *Earth*
888 *Planet. Sci. Lett.* 535, 116114. <https://doi.org/10.1016/j.epsl.2020.116114>
- 889 Graham, D.W., Hanan, B.B., Lupton, J.E., Hoernle, K., Werner, R., Christie, D.M., Sinton, J.M., 2014.
890 Helium Isotope Variations and Mantle Plume-Spreading Ridge Interactions Along the
891 Galápagos Spreading Center, in: Harpp, K.S., Mittelstaedt, E., d’Ozouville, N., Graham, D.W.
892 (Eds.), *Geophysical Monograph Series*. John Wiley & Sons, Inc, Hoboken, New Jersey, pp.
893 393–414. <https://doi.org/10.1002/9781118852538.ch18>
- 894 Hanan, B.B., Graham, D.W., 1996. Lead and Helium Isotope Evidence from Oceanic Basalts for a
895 Common Deep Source of Mantle Plumes. *Science* 272, 991–995.
896 <https://doi.org/10.1126/science.272.5264.991>
- 897 Harpp, K.S., Geist, D.J., Koleszar, A.M., Christensen, B., Lyons, J., Sabga, M., Rollins, N., 2014a. The
898 Geology and Geochemistry of Isla Floreana, Galápagos: A Different Type of Late-Stage Ocean
899 Island Volcanism, in: Harpp, K.S., Mittelstaedt, E., d’Ozouville, N., Graham, D.W. (Eds.),
900 *Geophysical Monograph Series*. John Wiley & Sons, Inc, Hoboken, New Jersey, pp. 71–117.
901 <https://doi.org/10.1002/9781118852538.ch6>
- 902 Harpp, K.S., Hall, P.S., Jackson, M.G., 2014b. Galápagos and Easter: A Tale of Two Hotspots, in:
903 Harpp, K.S., Mittelstaedt, E., d’Ozouville, N., Graham, D.W. (Eds.), *Geophysical Monograph*
904 *Series*. John Wiley & Sons, Inc, Hoboken, New Jersey, pp. 27–40.
905 <https://doi.org/10.1002/9781118852538.ch3>
- 906 Harpp, K.S., Weis, D., 2020. Insights Into the Origins and Compositions of Mantle Plumes: A
907 Comparison of Galápagos and Hawai’i. *Geochem. Geophys. Geosystems* 21.
908 <https://doi.org/10.1029/2019GC008887>
- 909 Harpp, K.S., White, W.M., 2001. Tracing a mantle plume: Isotopic and trace element variations of
910 Galápagos seamounts. *Geochem. Geophys. Geosystems* 2, n/a-n/a.
911 <https://doi.org/10.1029/2000GC000137>
- 912 Harpp, K.S., Wirth, K.R., Teasdale, R., Blair, S., Reed, L., Barr, J., Pistiner, J., Korich, D., 2014c. Plume-
913 Ridge Interaction in the Galápagos: Perspectives from Wolf, Darwin, and Genovesa Islands,
914 in: Harpp, K.S., Mittelstaedt, E., d’Ozouville, N., Graham, D.W. (Eds.), *Geophysical*

- 915 Monograph Series. John Wiley & Sons, Inc, Hoboken, New Jersey, pp. 285–334.
916 <https://doi.org/10.1002/9781118852538.ch15>
- 917 Hart, S.R., Hauri, E.H., Oschmann, L.A., Whitehead, J.A., 1992. Mantle Plumes and Entrainment:
918 Isotopic Evidence. *Science* 256, 517–520. <https://doi.org/10.1126/science.256.5056.517>
- 919 Hauri, E., Gaetani, G., Green, T., 2006. Partitioning of water during melting of the Earth's upper
920 mantle at H₂O-undersaturated conditions. *Earth Planet. Sci. Lett.* 248, 715–734.
921 <https://doi.org/10.1016/j.epsl.2006.06.014>
- 922 Herzberg, C., Asimow, P.D., 2008. Petrology of some oceanic island basalts: PRIMELT2.XLS software
923 for primary magma calculation. *Geochem. Geophys. Geosystems* 9, n/a-n/a.
924 <https://doi.org/10.1029/2008GC002057>
- 925 Hirth, G., Kohlstedt, D., 2003. Rheology of the upper mantle and the mantle wedge: A view from the
926 experimentalists, in: Eiler, J. (Ed.), *Geophysical Monograph Series*. American Geophysical
927 Union, Washington, D. C., pp. 83–105. <https://doi.org/10.1029/138GM06>
- 928 Hirth, G., Kohlstedt, D.L., 1996. Water in the oceanic upper mantle: implications for rheology, melt
929 extraction and the evolution of the lithosphere. *Earth Planet. Sci. Lett.* 144, 93–108.
930 [https://doi.org/10.1016/0012-821X\(96\)00154-9](https://doi.org/10.1016/0012-821X(96)00154-9)
- 931 Hoernle, K., Werner, R., Morgan, J.P., Garbe-Schönberg, D., Bryce, J., Mrazek, J., 2000. Existence of
932 complex spatial zonation in the Galápagos plume. *Geology* 28, 435.
933 [https://doi.org/10.1130/0091-7613\(2000\)28<435:EOCSZL>2.0.CO;2](https://doi.org/10.1130/0091-7613(2000)28<435:EOCSZL>2.0.CO;2)
- 934 Hooft, E.E.E., Toomey, D.R., Solomon, S.C., 2003. Anomalously thin transition zone beneath the
935 Galápagos hotspot. *Earth Planet. Sci. Lett.* 216, 55–64. [https://doi.org/10.1016/S0012-821X\(03\)00517-X](https://doi.org/10.1016/S0012-821X(03)00517-X)
- 937 Iacovino, K., Matthews, S., Wieser, P., Moore, G., Bégué, F., 2020. VESical Part I: An open-source
938 thermodynamic model engine for mixed volatile (H₂O-CO₂) solubility in silicate melts
939 (preprint). *Earth Sciences*. <https://doi.org/10.31223/X5D606>
- 940 Ingle, S., Ito, G., Mahoney, J.J., Chazey, W., Sinton, J., Rotella, M., Christie, D.M., 2010. Mechanisms
941 of geochemical and geophysical variations along the western Galápagos Spreading Center.
942 *Geochem. Geophys. Geosystems* 11, n/a-n/a. <https://doi.org/10.1029/2009GC002694>
- 943 Ito, G., Bianco, T., 2014. Patterns in Galápagos Magmatism Arising from the Upper Mantle Dynamics
944 of Plume-Ridge Interaction, in: Harpp, K.S., Mittelstaedt, E., d'Ozouville, N., Graham, D.W.
945 (Eds.), *Geophysical Monograph Series*. John Wiley & Sons, Inc, Hoboken, New Jersey, pp.
946 245–261. <https://doi.org/10.1002/9781118852538.ch13>
- 947 Ito, G., Lin, J., 1995. Oceanic spreading center–hotspot interactions: Constraints from along-isochron
948 bathymetric and gravity anomalies. *Geology* 23, 657. [https://doi.org/10.1130/0091-7613\(1995\)023<0657:OSCHIC>2.3.CO;2](https://doi.org/10.1130/0091-7613(1995)023<0657:OSCHIC>2.3.CO;2)
- 950 Ito, G., Lin, J., Gable, C.W., 1997. Interaction of mantle plumes and migrating mid-ocean ridges:
951 Implications for the Galápagos plume-ridge system. *J. Geophys. Res. Solid Earth* 102, 15403–
952 15417. <https://doi.org/10.1029/97JB01049>
- 953 Ito, G., Lin, J., Graham, D.W., 2003. Observational and theoretical studies of the dynamics of mantle
954 plume–mid-ocean ridge interaction. *Rev. Geophys.* 41.
955 <https://doi.org/10.1029/2002RG000117>
- 956 Ito, G., Mahoney, J.J., 2005. Flow and melting of a heterogeneous mantle: 1. Method and
957 importance to the geochemistry of ocean island and mid-ocean ridge basalts. *Earth Planet.*
958 *Sci. Lett.* 230, 29–46. <https://doi.org/10.1016/j.epsl.2004.10.035>
- 959 Jackson, M.G., Koga, K.T., Price, A., Konter, J.G., Koppers, A.A.P., Finlayson, V.A., Konrad, K., Hauri,
960 E.H., Kylander-Clark, A., Kelley, K.A., Kendrick, M.A., 2015. Deeply dredged submarine HIMU
961 glasses from the Tuvalu Islands, Polynesia: Implications for volatile budgets of recycled
962 oceanic crust. *Geochem. Geophys. Geosystems* 16, 3210–3234.
963 <https://doi.org/10.1002/2015GC005966>

- 964 Jarosewich, E., Nelen, J.A., Norberg, J.A., 1980. Reference Samples for Electron Microprobe
965 Analysis*. *Geostand. Geoanalytical Res.* 4, 43–47. [https://doi.org/10.1111/j.1751-](https://doi.org/10.1111/j.1751-908X.1980.tb00273.x)
966 908X.1980.tb00273.x
- 967 Johnson, E.A., 2006. 6. Water in Nominally Anhydrous Crustal Minerals: Speciation, Concentration,
968 and Geologic Significance, in: Keppler, H., Smyth, J.R. (Eds.), *Water in Nominally Anhydrous*
969 *Minerals*. De Gruyter, Berlin, Boston, pp. 117–154. [https://doi.org/10.1515/9781501509476-](https://doi.org/10.1515/9781501509476-010)
970 010
- 971 Katz, R.F., Spiegelman, M., Langmuir, C.H., 2003. A new parameterization of hydrous mantle melting.
972 *Geochem. Geophys. Geosystems* 4, n/a-n/a. <https://doi.org/10.1029/2002GC000433>
- 973 Katz, R.F., Weatherley, S.M., 2012. Consequences of mantle heterogeneity for melt extraction at
974 mid-ocean ridges. *Earth Planet. Sci. Lett.* 335–336, 226–237.
975 <https://doi.org/10.1016/j.epsl.2012.04.042>
- 976 Kelemen, P.B., Hirth, G., Shimizu, N., Spiegelman, M., Dick, H.J., 1997. A review of melt migration
977 processes in the adiabatically upwelling mantle beneath oceanic spreading ridges. *Philos.*
978 *Trans. R. Soc. Lond. Ser. Math. Phys. Eng. Sci.* 355, 283–318.
979 <https://doi.org/10.1098/rsta.1997.0010>
- 980 Keller, T., Katz, R.F., 2016. The Role of Volatiles in Reactive Melt Transport in the Asthenosphere. *J.*
981 *Petrol.* 57, 1073–1108. <https://doi.org/10.1093/petrology/egw030>
- 982 Kendrick, M.A., Hémond, C., Kamenetsky, V.S., Danyushevsky, L., Devey, C.W., Rodemann, T.,
983 Jackson, M.G., Perfit, M.R., 2017. Seawater cycled throughout Earth’s mantle in partially
984 serpentinized lithosphere. *Nat. Geosci.* 10, 222–228. <https://doi.org/10.1038/ngeo2902>
- 985 Kendrick, M.A., Jackson, M.G., Hauri, E.H., Phillips, D., 2015. The halogen (F, Cl, Br, I) and H₂O
986 systematics of Samoan lavas: Assimilated-seawater, EM2 and high-3He/4He components.
987 *Earth Planet. Sci. Lett.* 410, 197–209. <https://doi.org/10.1016/j.epsl.2014.11.026>
- 988 Kingsley, R.H., Schilling, J.-G., 1998. Plume-ridge interaction in the Easter-Salas y Gomez seamount
989 chain-Easter Microplate system: Pb isotope evidence. *J. Geophys. Res. Solid Earth* 103,
990 24159–24177. <https://doi.org/10.1029/98JB01496>
- 991 Kokfelt, T., Lundstrom, C., Hoernle, K., Hauff, F., Werner, R., 2005. Plume–ridge interaction studied
992 at the Galápagos spreading center: Evidence from 226Ra–230Th–238U and 231Pa–235U
993 isotopic disequilibria. *Earth Planet. Sci. Lett.* 234, 165–187.
994 <https://doi.org/10.1016/j.epsl.2005.02.031>
- 995 Koleszar, A.M., Saal, A.E., Hauri, E.H., Nagle, A.N., Liang, Y., Kurz, M.D., 2009. The volatile contents of
996 the Galapagos plume; evidence for H₂O and F open system behavior in melt inclusions.
997 *Earth Planet. Sci. Lett.* 287, 442–452. <https://doi.org/10.1016/j.epsl.2009.08.029>
- 998 Kurz, M.D., Curtice, J., Fornari, D., Geist, D., Moreira, M., 2009. Primitive neon from the center of the
999 Galápagos hotspot. *Earth Planet. Sci. Lett.* 286, 23–34.
1000 <https://doi.org/10.1016/j.epsl.2009.06.008>
- 1001 Kurz, M.D., Geist, D., 1999. Dynamics of the Galapagos hotspot from helium isotope geochemistry.
1002 *Geochim. Cosmochim. Acta* 63, 4139–4156. [https://doi.org/10.1016/S0016-7037\(99\)00314-](https://doi.org/10.1016/S0016-7037(99)00314-2)
1003 2
- 1004 Lambart, S., 2017. No direct contribution of recycled crust in Icelandic basalts. *Geochem. Perspect.*
1005 *Lett.* 7–12. <https://doi.org/10.7185/geochemlet.1728>
- 1006 Langmuir, C.H., Bender, J.F., 1984. The geochemistry of oceanic basalts in the vicinity of transform
1007 faults: Observations and implications. *Earth Planet. Sci. Lett.* 69, 107–127.
1008 [https://doi.org/10.1016/0012-821X\(84\)90077-3](https://doi.org/10.1016/0012-821X(84)90077-3)
- 1009 Le Roux, P., Shirey, S., Hauri, E., Perfit, M., Bender, J., 2006. The effects of variable sources,
1010 processes and contaminants on the composition of northern EPR MORB (8–10°N and 12–
1011 14°N): Evidence from volatiles (H₂O, CO₂, S) and halogens (F, Cl). *Earth Planet. Sci. Lett.* 251,
1012 209–231. <https://doi.org/10.1016/j.epsl.2006.09.012>
- 1013 Le Voyer, M., Cottrell, E., Kelley, K.A., Brounce, M., Hauri, E.H., 2015. The effect of primary versus
1014 secondary processes on the volatile content of MORB glasses: An example from the

- 1015 equatorial Mid-Atlantic Ridge (5°N-3°S): MORB volatile contents along 5{degree sign}N-
1016 3{degree sign}S MAR. *J. Geophys. Res. Solid Earth* 120, 125–144.
1017 <https://doi.org/10.1002/2014JB011160>
- 1018 Le Voyer, M., Hauri, E.H., Cottrell, E., Kelley, K.A., Salters, V.J.M., Langmuir, C.H., Hilton, D.R., Barry,
1019 P.H., Füre, E., 2018. Carbon fluxes and primary magma CO₂ contents along the global mid-
1020 ocean ridge system. *Geochem. Geophys. Geosystems*.
1021 <https://doi.org/10.1029/2018GC007630>
- 1022 MacLennan, J., McKenzie, D., Gronvöld, K., 2001. Plume-driven upwelling under central Iceland. *Earth*
1023 *Planet. Sci. Lett.* 194, 67–82. [https://doi.org/10.1016/S0012-821X\(01\)00553-2](https://doi.org/10.1016/S0012-821X(01)00553-2)
- 1024 Marks, M.A.W., Kendrick, M.A., Eby, G.N., Zack, T., Wenzel, T., 2017. The F, Cl, Br and I Contents of
1025 Reference Glasses BHVO-2G, BIR-1G, BCR-2G, GSD-1G, GSE-1G, NIST SRM 610 and NIST SRM
1026 612. *Geostand. Geoanalytical Res.* 41, 107–122. <https://doi.org/10.1111/ggr.12128>
- 1027 Matthews, S., Shorttle, O., Wong, K., 2020. *simonwmatthews/pyMelt: First Release*. Zenodo.
1028 <https://doi.org/10.5281/ZENODO.4011814>
- 1029 Métrich, N., Zanon, V., Créon, L., Hildenbrand, A., Moreira, M., Marques, F.O., 2014. Is the ‘Azores
1030 Hotspot’ a Wetspot? Insights from the Geochemistry of Fluid and Melt Inclusions in Olivine
1031 of Pico Basalts. *J. Petrol.* 55, 377–393. <https://doi.org/10.1093/petrology/egt071>
- 1032 Michael, P., 1995. Regionally distinctive sources of depleted MORB: Evidence from trace elements
1033 and H₂O. *Earth Planet. Sci. Lett.* 131, 301–320. [https://doi.org/10.1016/0012-
1034 821X\(95\)00023-6](https://doi.org/10.1016/0012-821X(95)00023-6)
- 1035 Michael, P.J., 1999. Implications for magmatic processes at Ontong Java Plateau from volatile and
1036 major element contents of Cretaceous basalt glasses. *Geochem Geophys Geosyst* 1.
- 1037 Michael, P.J., 1988. The concentration, behavior and storage of H₂O in the suboceanic upper mantle:
1038 Implications for mantle metasomatism. *Geochim. Cosmochim. Acta* 52, 555–566.
1039 [https://doi.org/10.1016/0016-7037\(88\)90110-X](https://doi.org/10.1016/0016-7037(88)90110-X)
- 1040 Michael, P.J., Cornell, W.C., 1998. Influence of spreading rate and magma supply on crystallization
1041 and assimilation beneath mid-ocean ridges: Evidence from chlorine and major element
1042 chemistry of mid-ocean ridge basalts. *J. Geophys. Res. Solid Earth* 103, 18325–18356.
1043 <https://doi.org/10.1029/98JB00791>
- 1044 Mittal, T., Richards, M.A., 2017. Plume-ridge interaction via melt channelization at Galápagos and
1045 other near-ridge hotspot provinces. *Geochem. Geophys. Geosystems* 18, 1711–1738.
1046 <https://doi.org/10.1002/2016GC006454>
- 1047 Mittelstaedt, E., Soule, A.S., Harpp, K.S., Fornari, D., 2014. Variations in Crustal Thickness, Plate
1048 Rigidity, and Volcanic Processes Throughout the Northern Galápagos Volcanic Province, in:
1049 Harpp, K.S., Mittelstaedt, E., d’Ozouville, N., Graham, D.W. (Eds.), *Geophysical Monograph*
1050 *Series*. John Wiley & Sons, Inc, Hoboken, New Jersey, pp. 263–284.
1051 <https://doi.org/10.1002/9781118852538.ch14>
- 1052 Morgan, W.J., 1978. Rodriguez, Darwin, Amsterdam, ..., A second type of Hotspot Island. *J. Geophys.*
1053 *Res.* 83, 5355. <https://doi.org/10.1029/JB083iB11p05355>
- 1054 Morgan, W.J., 1971. Convection Plumes in the Lower Mantle. *Nature* 230, 42–43.
1055 <https://doi.org/10.1038/230042a0>
- 1056 Peterson, M.E., Saal, A.E., Kurz, M.D., Hauri, E.H., Blusztajn, J.S., Harpp, K.S., Werner, R., Geist, D.J.,
1057 2017. Submarine Basaltic Glasses from the Galapagos Archipelago: Determining the Volatile
1058 Budget of the Mantle Plume. *J. Petrol.* 58, 1419–1450.
1059 <https://doi.org/10.1093/petrology/egx059>
- 1060 Reekie, C.D.J., Jenner, F.E., Smythe, D.J., Hauri, E.H., Bullock, E.S., Williams, H.M., 2019. Sulfide
1061 resorption during crustal ascent and degassing of oceanic plateau basalts. *Nat. Commun.* 10.
1062 <https://doi.org/10.1038/s41467-018-08001-3>
- 1063 Ribe, N.M., 1996. The dynamics of plume-ridge interaction: 2. Off-ridge plumes. *J. Geophys. Res.*
1064 *Solid Earth* 101, 16195–16204. <https://doi.org/10.1029/96JB01187>

- 1065 Rosenthal, A., Hauri, E.H., Hirschmann, M.M., 2015. Experimental determination of C, F, and H
1066 partitioning between mantle minerals and carbonated basalt, CO₂/Ba and CO₂/Nb
1067 systematics of partial melting, and the CO₂ contents of basaltic source regions. *Earth Planet.*
1068 *Sci. Lett.* 412, 77–87. <https://doi.org/10.1016/j.epsl.2014.11.044>
- 1069 Ryan, W.B.F., Carbotte, S.M., Coplan, J.O., O'Hara, S., Melkonian, A., Arko, R., Weissel, R.A., Ferrini,
1070 V., Goodwillie, A., Nitsche, F., Bonczkowski, J., Zemsky, R., 2009. Global Multi-Resolution
1071 Topography synthesis. *Geochem. Geophys. Geosystems* 10, n/a-n/a.
1072 <https://doi.org/10.1029/2008GC002332>
- 1073 Saal, A.E., Hauri, E.H., Langmuir, C.H., Perfit, M.R., 2002. Vapour undersaturation in primitive mid-
1074 ocean-ridge basalt and the volatile content of Earth's upper mantle. *Nature* 419, 451–455.
1075 <https://doi.org/10.1038/nature01073>
- 1076 Salters, V.J.M., Stracke, A., 2004. Composition of the depleted mantle. *Geochem. Geophys.*
1077 *Geosystems* 5, n/a-n/a. <https://doi.org/10.1029/2003GC000597>
- 1078 Schilling, J.-G., 1991. Fluxes and excess temperatures of mantle plumes inferred from their
1079 interaction with migrating mid-ocean ridges. *Nature* 352, 397–403.
1080 <https://doi.org/10.1038/352397a0>
- 1081 Schilling, J.-G., Fontignie, D., Blichert-Toft, J., Kingsley, R., Tomza, U., 2003. Pb-Hf-Nd-Sr isotope
1082 variations along the Galápagos Spreading Center (101°-83°W): Constraints on the dispersal
1083 of the Galápagos mantle plume. *Geochem. Geophys. Geosystems* 4.
1084 <https://doi.org/10.1029/2002GC000495>
- 1085 Schilling, J.-G., Kingsley, R.H., Devine, J.D., 1982. Galapagos Hot Spot-Spreading Center System: 1.
1086 Spatial petrological and geochemical variations (83°W-101°W). *J. Geophys. Res. Solid Earth*
1087 87, 5593–5610. <https://doi.org/10.1029/JB087iB07p05593>
- 1088 Shimizu, K., Ito, M., Chang, Q., Miyazaki, T., Ueki, K., Toyama, C., Senda, R., Vaglarov, B.S., Ishikawa,
1089 T., Kimura, J.-I., 2019. Identifying volatile mantle trend with the water–fluorine–cerium
1090 systematics of basaltic glass. *Chem. Geol.* 522, 283–294.
1091 <https://doi.org/10.1016/j.chemgeo.2019.06.014>
- 1092 Shimizu, K., Saal, A.E., Myers, C.E., Nagle, A.N., Hauri, E.H., Forsyth, D.W., Kamenetsky, V.S., Niu, Y.,
1093 2016. Two-component mantle melting-mixing model for the generation of mid-ocean ridge
1094 basalts: Implications for the volatile content of the Pacific upper mantle. *Geochim.*
1095 *Cosmochim. Acta* 176, 44–80. <https://doi.org/10.1016/j.gca.2015.10.033>
- 1096 Shishkina, T.A., Botcharnikov, R.E., Holtz, F., Almeev, R.R., Jazwa, A.M., Jakubiak, A.A., 2014.
1097 Compositional and pressure effects on the solubility of H₂O and CO₂ in mafic melts. *Chem.*
1098 *Geol.* 388, 112–129. <https://doi.org/10.1016/j.chemgeo.2014.09.001>
- 1099 Shishkina, T.A., Botcharnikov, R.E., Holtz, F., Almeev, R.R., Portnyagin, M.V., 2010. Solubility of H₂O-
1100 and CO₂-bearing fluids in tholeiitic basalts at pressures up to 500MPa. *Chem. Geol.* 277,
1101 115–125. <https://doi.org/10.1016/j.chemgeo.2010.07.014>
- 1102 Shorttle, O., MacLennan, J., Jones, S.M., 2010. Control of the symmetry of plume-ridge interaction by
1103 spreading ridge geometry. *Geochem. Geophys. Geosystems* 11, n/a-n/a.
1104 <https://doi.org/10.1029/2009GC002986>
- 1105 Sinton, J., Detrick, R., Canales, J.P., Ito, G., Behn, M., 2003. Morphology and segmentation of the
1106 western Galápagos Spreading Center, 90.5°-98°W: Plume-ridge interaction at an
1107 intermediate spreading ridge. *Geochem. Geophys. Geosystems* 4.
1108 <https://doi.org/10.1029/2003GC000609>
- 1109 Sinton, J.M., Detrick, R.S., 1992. Mid-ocean ridge magma chambers. *J. Geophys. Res.* 97, 197.
1110 <https://doi.org/10.1029/91JB02508>
- 1111 Sleep, N.H., 1990. Hotspots and mantle plumes: Some phenomenology. *J. Geophys. Res.* 95, 6715.
1112 <https://doi.org/10.1029/JB095iB05p06715>
- 1113 Sobolev, A.V., Hofmann, A.W., Kuzmin, D.V., Yaxley, G.M., Arndt, N.T., Chung, S.-L., Danyushevsky,
1114 L.V., Elliott, T., Frey, F.A., Garcia, M.O., Gurenko, A.A., Kamenetsky, V.S., Kerr, A.C.,
1115 Krivolutsкая, N.A., Matvienkov, V.V., Nikogosian, I.K., Rocholl, A., Sigurdsson, I.A.,

- 1116 Sushchevskaya, N.M., Teklay, M., 2007. The Amount of Recycled Crust in Sources of Mantle-
1117 Derived Melts 316, 7.
- 1118 Sorbadere, F., Médard, E., Laporte, D., Schiano, P., 2013. Experimental melting of hydrous
1119 peridotite–pyroxenite mixed sources: Constraints on the genesis of silica-undersaturated
1120 magmas beneath volcanic arcs. *Earth Planet. Sci. Lett.* 15.
- 1121 Stroncik, N.A., Devey, C.W., 2011. Recycled gabbro signature in hotspot magmas unveiled by plume–
1122 ridge interactions. *Nat. Geosci.* 4, 393–397. <https://doi.org/10.1038/ngeo1121>
- 1123 Stroncik, N.A., Niedermann, S., Haase, K.M., 2008. Plume–ridge interaction revisited: Evidence for
1124 melt mixing from He, Ne and Ar isotope and abundance systematics. *Earth Planet. Sci. Lett.*
1125 268, 424–432. <https://doi.org/10.1016/j.epsl.2008.01.037>
- 1126 Sun, Z., Xiong, X., Wang, J., Liu, X., Li, L., Ruan, M., Zhang, L., Takahashi, E., 2020. Sulfur abundance
1127 and heterogeneity in the MORB mantle estimated by copper partitioning and sulfur
1128 solubility modelling. *Earth Planet. Sci. Lett.* 538, 116169.
1129 <https://doi.org/10.1016/j.epsl.2020.116169>
- 1130 Verma, S.P., Schilling, J.-G., 1982. Galapagos Hot Spot-SPreading Center System: 2. ⁸⁷SR/ ⁸⁶SR and
1131 large ion lithophile element variations (85°W–101°W). *J. Geophys. Res. Solid Earth* 87,
1132 10838–10856. <https://doi.org/10.1029/JB087iB13p10838>
- 1133 Vidito, C., Herzberg, C., Gazel, E., Geist, D., Harpp, K., 2013. Lithological structure of the Galápagos
1134 Plume: Lithological Structure Galpagos Plume. *Geochem. Geophys. Geosystems* 14, 4214–
1135 4240. <https://doi.org/10.1002/ggge.20270>
- 1136 Villagómez, D.R., Toomey, D.R., Geist, D.J., Hooft, E.E.E., Solomon, S.C., 2014. Mantle flow and
1137 multistage melting beneath the Galápagos hotspot revealed by seismic imaging. *Nat. Geosci.*
1138 7, 151–156. <https://doi.org/10.1038/ngeo2062>
- 1139 Weatherley, S.M., Katz, R.F., 2012. Melting and channelized magmatic flow in chemically
1140 heterogeneous, upwelling mantle. *Geochem. Geophys. Geosystems* 13.
1141 <https://doi.org/10.1029/2011GC003989>
- 1142 Weatherley, S.M., Katz, R.F., 2010. Plate-driven mantle dynamics and global patterns of mid-ocean
1143 ridge bathymetry. *Geochem. Geophys. Geosystems* 11, n/a-n/a.
1144 <https://doi.org/10.1029/2010GC003192>
- 1145 Weis, D., Garcia, M.O., Rhodes, J.M., Jellinek, M., Scoates, J.S., 2011. Role of the deep mantle in
1146 generating the compositional asymmetry of the Hawaiian mantle plume. *Nat. Geosci.* 4,
1147 831–838. <https://doi.org/10.1038/ngeo1328>
- 1148 White, W.M., McBirney, A.R., Duncan, R.A., 1993. Petrology and geochemistry of the Galápagos
1149 Islands: Portrait of a pathological mantle plume. *J. Geophys. Res. Solid Earth* 98, 19533–
1150 19563. <https://doi.org/10.1029/93JB02018>
- 1151 Wieser, P.E., Jenner, F., Edmonds, M., Maclennan, J., Kunz, B.E., 2020. Chalcophile elements track
1152 the fate of sulfur at Kīlauea Volcano, Hawai‘i. *Geochim. Cosmochim. Acta*
1153 S0016703720303239. <https://doi.org/10.1016/j.gca.2020.05.018>
- 1154 Workman, R.K., Hart, S.R., 2005. Major and trace element composition of the depleted MORB
1155 mantle (DMM). *Earth Planet. Sci. Lett.* 231, 53–72.
1156 <https://doi.org/10.1016/j.epsl.2004.12.005>
- 1157 Workman, R.K., Hauri, E., Hart, S.R., Wang, J., Blusztajn, J., 2006. Volatile and trace elements in
1158 basaltic glasses from Samoa: Implications for water distribution in the mantle. *Earth Planet.*
1159 *Sci. Lett.* 241, 932–951. <https://doi.org/10.1016/j.epsl.2005.10.028>
- 1160

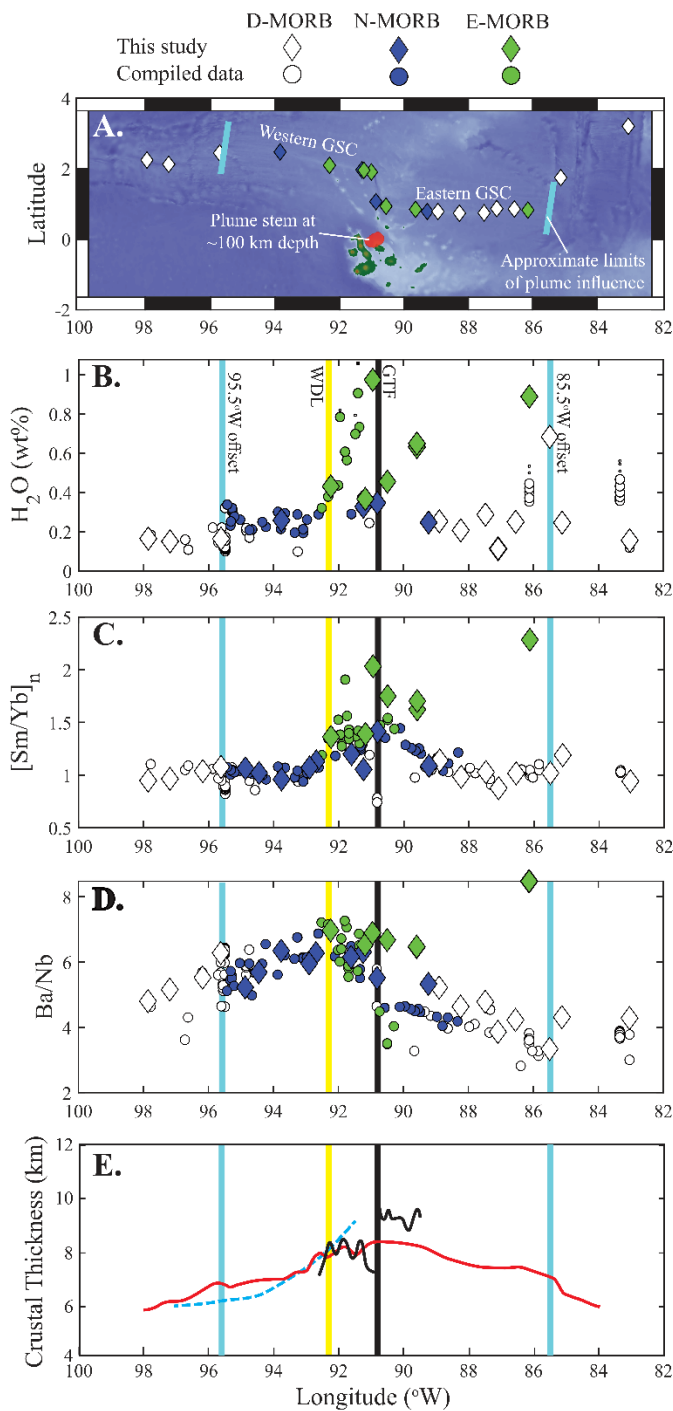
1161 SUPPLEMENTARY REFERENCES

- 1162 Connolly, J. (2009). The geodynamic equation of state: what and how. *Geochemistry, Geophysics,*
1163 *Geosystems*, 10 (10).

This represents a post-print of a peer-reviewed manuscript that has been accepted for publication in *Geochemistry, Geophysics, Geosystems* (acceptance date 19/10/2021).

- 1164 Hanyu, T., Shimizu, K., Ushikubo, T., Kimura, J.-I., Chang, Q., Hamada, M., & Ishikawa, T. (2019). Tiny
1165 droplets of ocean island basalts unveil Earth's deep chlorine cycle. *Nature communications*,
1166 10 (1), 60.
- 1167 Holland, T. J., Green, E. C., & Powell, R. (2018). Melting of peridotites through to granites: a simple
1168 thermodynamic model in the system KNCFMASHTOCr. *Journal of Petrology*, 59 (5), 881{900}.
- 1169 Jennings, E. S., & Holland, T. J. (2015). A simple thermodynamic model for melting of peridotite in
1170 the system NCFMASOCr. *Journal of Petrology*, 56 (5), 869{892}.
- 1171 Kendrick, M. A., Jackson, M. G., Kent, A. J., Hauri, E. H., Wallace, P. J., & Woodhead, J. (2014).
1172 Contrasting behaviours of CO₂, S, H₂O and halogens (F, Cl, Br, and I) in enriched-mantle melts
1173 from Pitcairn and Society seamounts. *Chemical Geology*, 370, 69{81}.
- 1174 Matthews, S., Wong, K., Shorttle, O., Edmonds, M., & Maclennan, J. (2021). Do olivine crystallization
1175 temperatures faithfully record mantle temperature variability? *Geochemistry, Geophysics,*
1176 *Geosystems*, 22 (4), e2020GC009157.
- 1177 Miller, W. G., Maclennan, J., Shorttle, O., Gaetani, G. A., Le Roux, V., & Klein, F. (2019). Estimating
1178 the carbon content of the deep mantle with Icelandic melt inclusions. *Earth and Planetary*
1179 *Science Letters*, 523.
- 1180 Rudge, J. F., Maclennan, J., & Stracke, A. (2013). The geochemical consequences of mixing melts
1181 from a heterogeneous mantle. *Geochimica et Cosmochimica Acta*, 114, 112{143}.

1182 **FIGURES**



1183

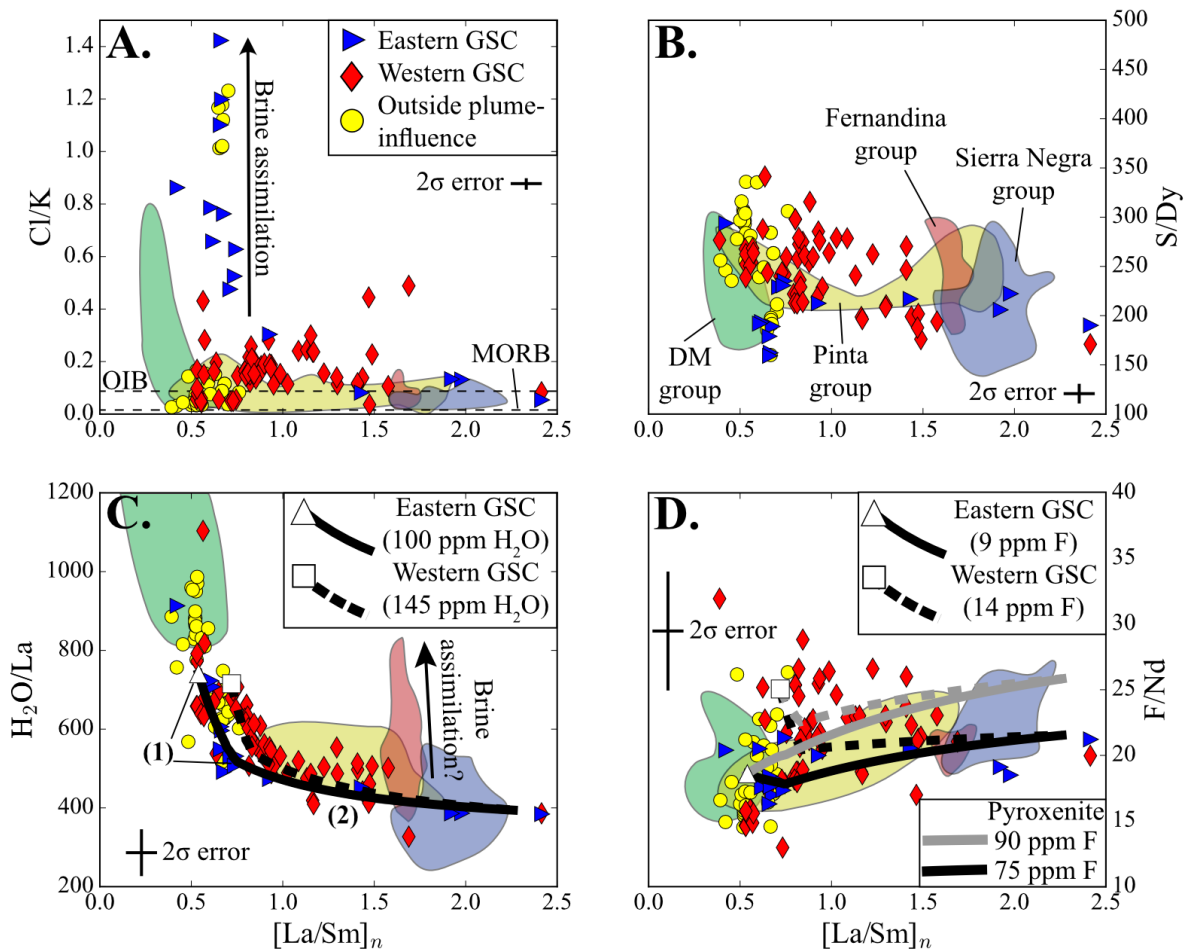
1184 **Figure 1** – Location and chemistry of the basalts from the GSC. **A.** Map of the Galápagos Spreading

1185 Centre (GSC) and Galápagos Archipelago (bathymetric data from Ryan et al., 2009). **B.** Brine-

1186 assimilation corrected H₂O contents in the GSC basalts from this study (diamonds) and from

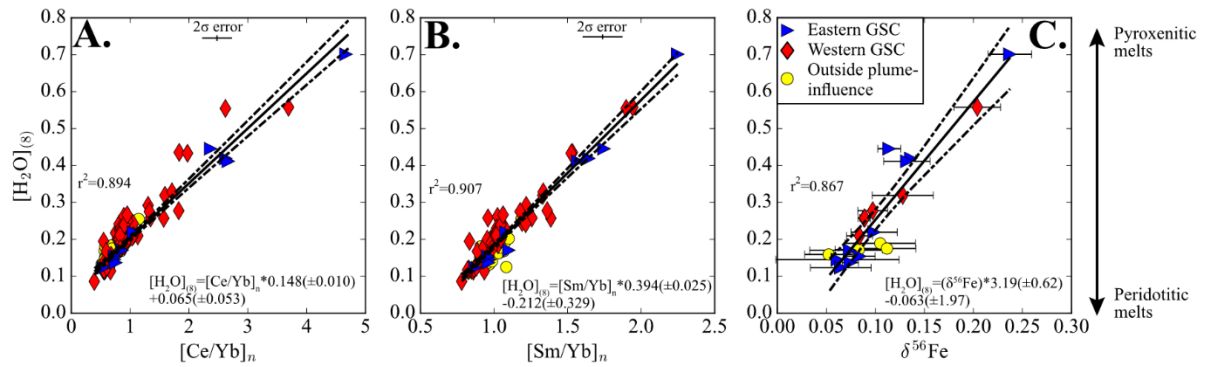
1187 Cushman et al. (2004) and Le Voyer et al. (2018; circles). The measured H₂O contents of these

1188 basalts are shown by the small dots (only visible where large differences between the measured and
1189 corrected H₂O concentrations are seen; Supplementary Information). Panels C. and D. show key
1190 trace element ratios ([Sm/Yb]_n and Ba/Nb, respectively), which display an increased contribution
1191 from melts of a garnet-bearing lithology near the Galápagos Transform Fault (GTF; C.); and a
1192 geochemical offset between the western and eastern GSC, which relates to the incorporation of the
1193 Wolf-Darwin component in the mantle beneath the western GSC (D.; data from Christie et al., 2005;
1194 Gleeson et al., 2020; Ingle et al., 2010). Crustal thickness estimates are shown in panel E. from Ito
1195 and Lin (1995; red), Canales et al. (2002; blue), and Mittelstaedt et al. (2014; black). 2σ error is
1196 smaller than the symbol size for all graphs. Yellow line represents the intersection of the Wolf-
1197 Darwin Lineament with the GSC. The blue lines represent the approximate limit of plume influence
1198 along the GSC.



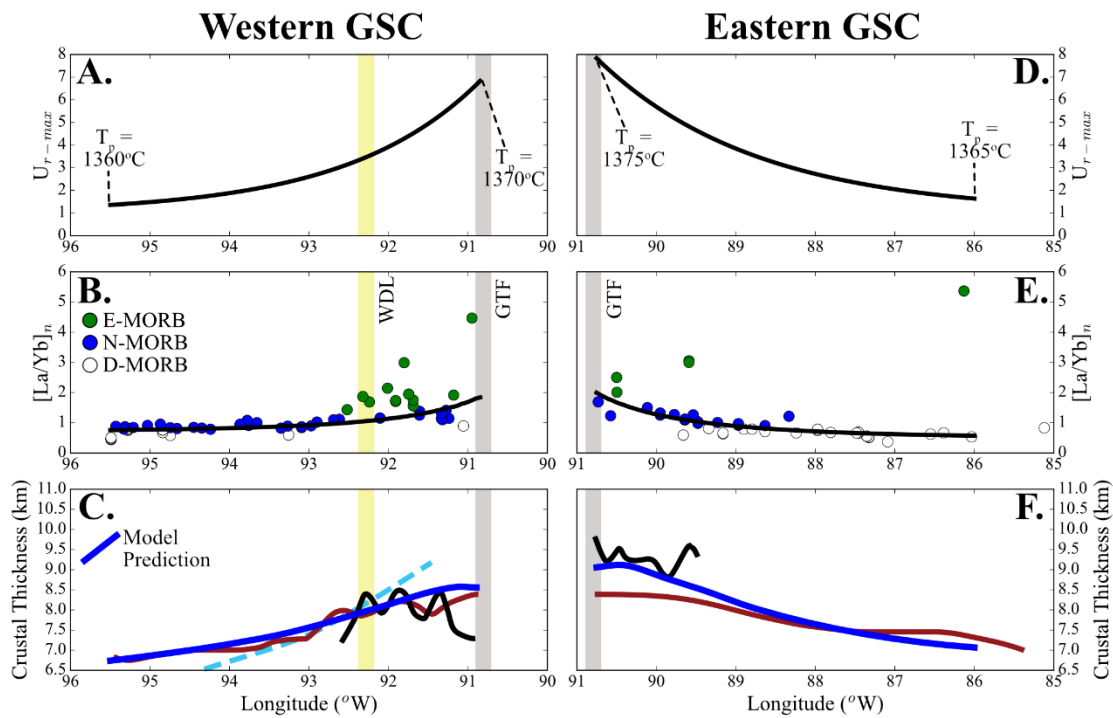
This represents a post-print of a peer-reviewed manuscript that has been accepted for publication in *Geochemistry, Geophysics, Geosystems* (acceptance date 19/10/2021).

1200 **Figure 2** – Relationship between volatile to non-volatile trace element ratios (e.g. H₂O/La) and
1201 indices of enrichment (represented here by [La/Sm]_n). Shown in all panels are the composition of the
1202 GSC basalts (colour coded according to location) as well as the composition of submarine basalts
1203 from the Galápagos Archipelago measured by Peterson et al. (2017). **A.** Many of the GSC basalts
1204 contain higher Cl/K ratios than those typically seen in MORBs or OIBs. Fernandina melt inclusions
1205 have Cl/K ratios of ~0.038 (Koleszar et al. 2009). **B.** The S/Dy ratios of GSC basalts are similar to those
1206 observed in basaltic glass chips from across the archipelago (Peterson et al., 2017). **C.** The H₂O/La
1207 ratio of plume-influenced GSC basalts varies from ~750 in depleted samples to <400 in the enriched
1208 samples. The white symbols and black lines show the compositions predicted by mantle melting
1209 models in this study. In the region labelled **(1)**, the black lines display the influence of increasing the
1210 amount of pyroxenitic material in the mantle source beneath the GSC (up to 8%, consistent with the
1211 models shown in Fig. 5). Region **(2)** displays the influence of increasing the contribution of
1212 channelised, plume-derived melts from a pyroxenitic source with ~550 ppm H₂O. The H₂O data from
1213 the GSC has been corrected for the influence of brine assimilation whereas the data for the
1214 submarine basalts from Peterson et al. (2017) has not (as different correction factors are required
1215 for each dataset). **D.** Black lines show the model predictions for increasing contribution of
1216 channelised flow where the enriched mantle end-member contains 75 ppm F. Grey lines show
1217 equivalent models for a scenario where the enriched, pyroxenitic end-member contains 90 ppm F.
1218 GSC data taken from this study (eastern GSC), Ingle et al. (2010), Cushman et al. (2004) and Le Voyer
1219 et al. (2018).



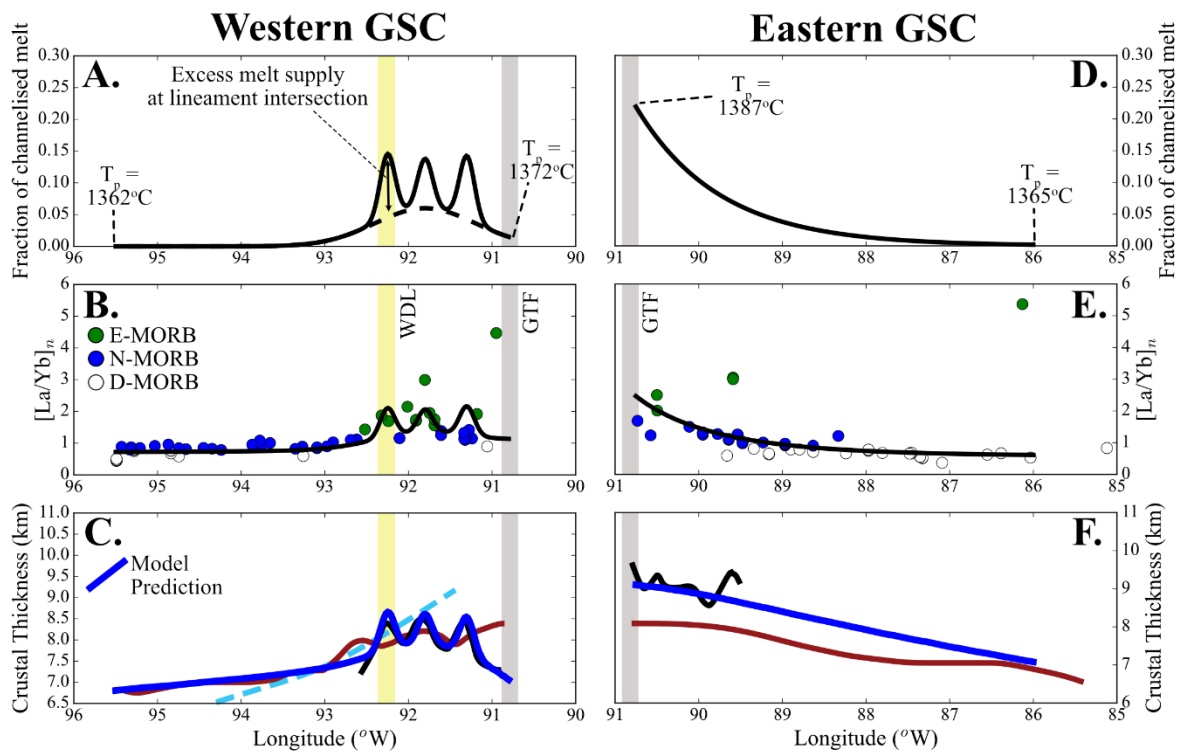
1220

1221 **Figure 3** – Relationship between $[H_2O]_{(8)}$ and key geochemical indices of compositional enrichment.
 1222 **A.** and **B.** display the correlation between trace element proxies of geochemical enrichment/melt
 1223 fraction and $[H_2O]_{(8)}$ (fractionation corrected H_2O). The correlation between $[Sm/Yb]_n$ and $[H_2O]_{(8)}$
 1224 (**A.**) is used to predict the fractionation corrected H_2O concentration of the GSC basalts for which
 1225 volatile data does not exist. The data displayed here has been corrected for the influence of brine
 1226 assimilation (Supplementary Information). **C.** A strong correlation is observed between $\delta^{56}Fe$ and
 1227 $[H_2O]_{(8)}$, which indicates that there is a contribution of volatile-rich, pyroxenitic melts to the GSC
 1228 basalts. Fe-isotope data from Gleeson et al. (2020), trace element and volatile element data from
 1229 this study; Cushman et al. (2004); Gleeson et al. (2020); Ingle et al. (2010); and Le Voyer et al. (2018).



1230

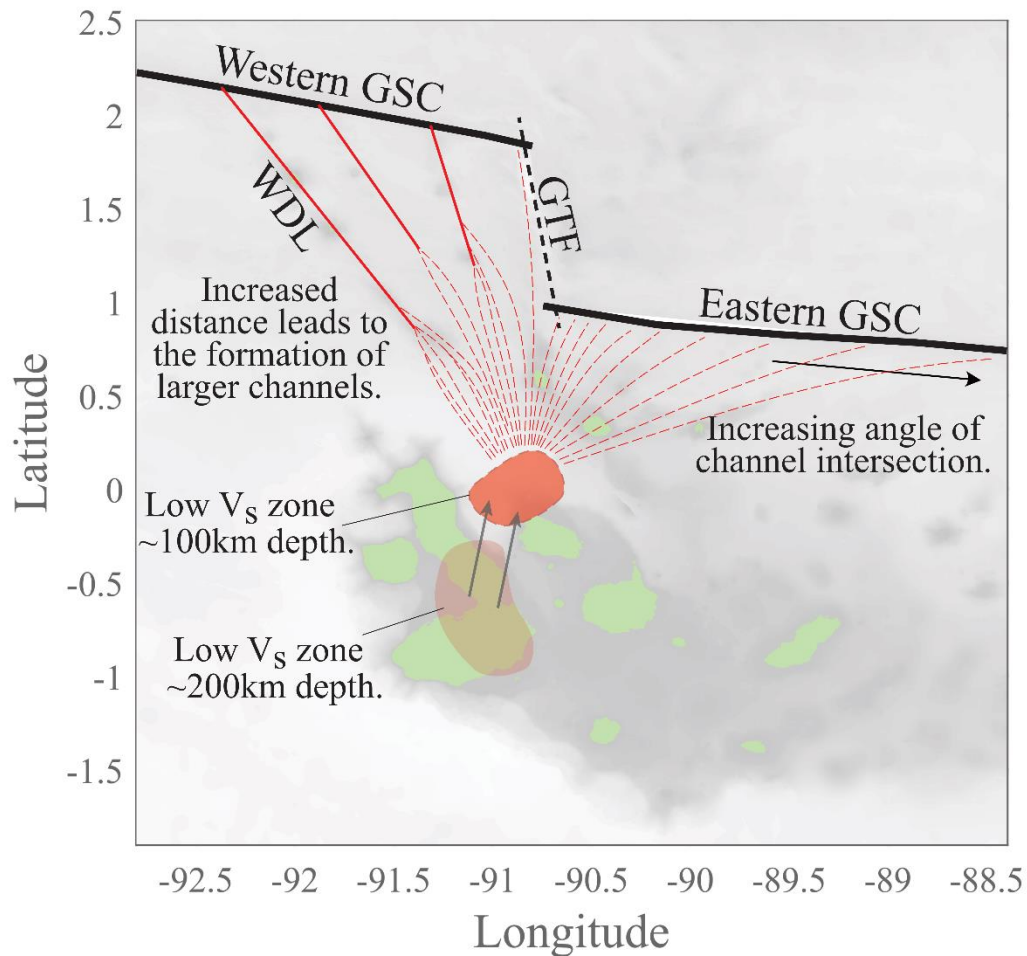
1231 **Figure 4** – Results of plume-ridge interaction models that only account for solid-state transport
 1232 between the Galápagos mantle plume and the GSC. Panels **A.** - **C.** show the results for the western
 1233 GSC and panels **D.** - **F.** show the results for the eastern GSC. Panels **A.** and **D.** show the input
 1234 parameters for these models, and the geochemical (**B.** and **E.**) and crustal thickness (**C.** and **F.**)
 1235 results are shown below. Black lines in **B.** and **E.** display the mean composition of melts delivered to
 1236 that section of ridge. Crustal thickness estimates are from Ito and Lin (1995; red), Canales et al.
 1237 (2002; blue dashed), and Mittelstaedt et al. (2014; black); modelled crustal thickness is shown in
 1238 blue (solid line). Some of the long length-scale trends in geochemical enrichment are reproduced
 1239 along the GSC; however, several discrepancies can be observed between the model predictions and
 1240 the crustal thickness and geochemical data from the GSC.



1241

1242 **Figure 5** - Results of plume-ridge interaction models that account for channelised melt transport
 1243 between the Galápagos mantle plume and the GSC. Panels **A. - C.** show the results for the western
 1244 GSC and panels **D. - F.** show the results for the eastern GSC. Panels **A.** and **D.** show the input
 1245 parameters for these models (i.e. the fraction of channelised melt), and the geochemical (**B.** and **E.**)
 1246 and crustal thickness (**C.** and **F.**) results are shown below. Crustal thickness estimates are from Ito
 1247 and Lin (1995; red), Canales et al. (2002; blue dashed), and Mittelstaedt et al. (2014; black);
 1248 modelled crustal thickness is shown in blue (solid line). It can be observed that, by assuming
 1249 channelised flow occurs beneath the volcanic lineaments of the Northern Galápagos Volcanic
 1250 Province, the crustal thickness and geochemical signature of the basalts from the western GSC are
 1251 more accurately reproduced in this model than in the model of solid-state plume-ridge interaction
 1252 shown in Fig. 4.

1253

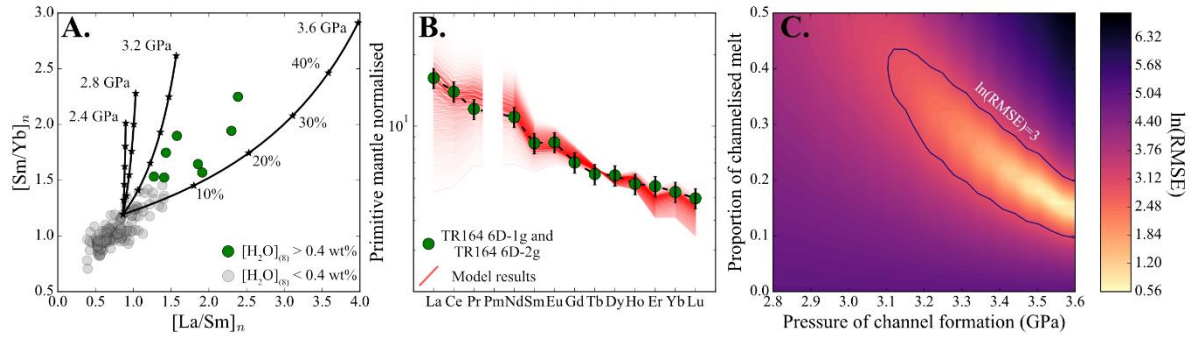


1254

1255 **Figure 6** – Schematic diagram illustrating the nature of the melt channels beneath the northern
1256 Galápagos volcanic province. The eastern GSC is fed by a large number of small melt channels and
1257 the influence of these melt channels declines with increasing distance to the mantle plume. On the
1258 western GSC our models predict that the melt channels amalgamate into three larger channels that
1259 are located beneath each of the three volcanic lineaments in the northern Galápagos volcanic
1260 province. The location of the Galápagos mantle plume at depths of 200 and 100 km is taken from
1261 Villagómez et al. (2014).

1262

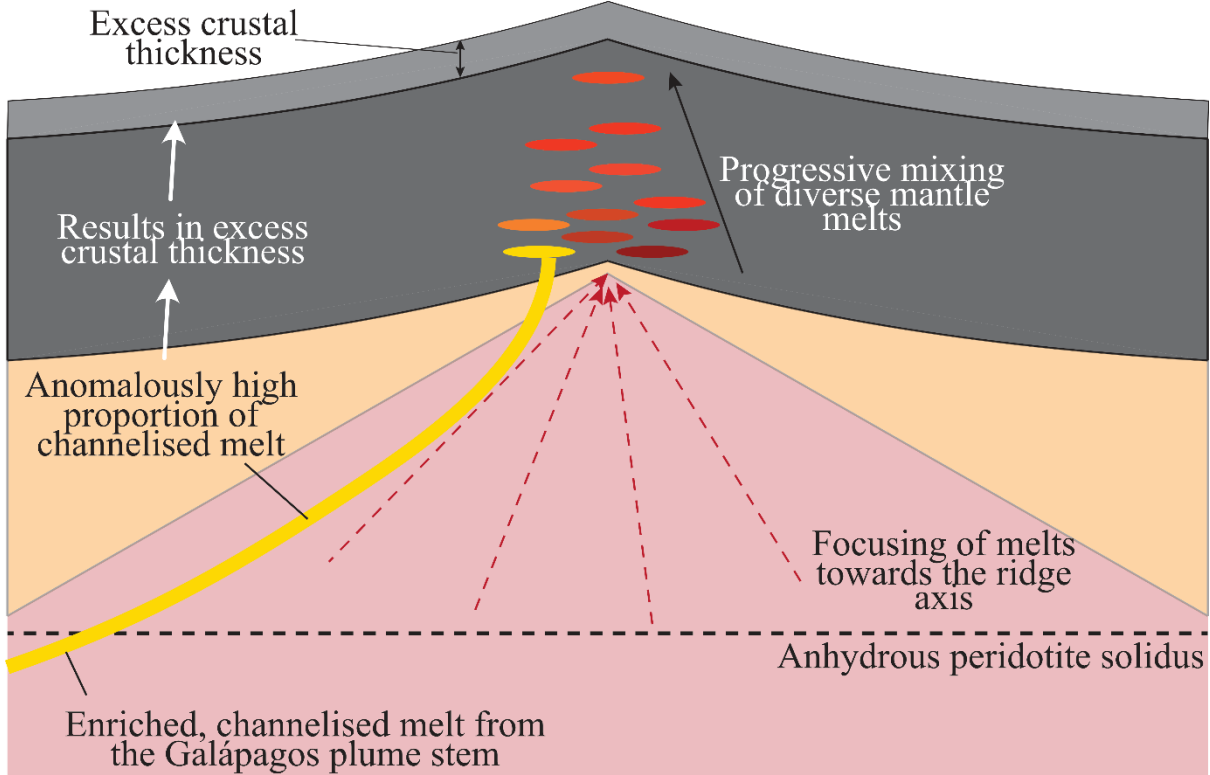
1263



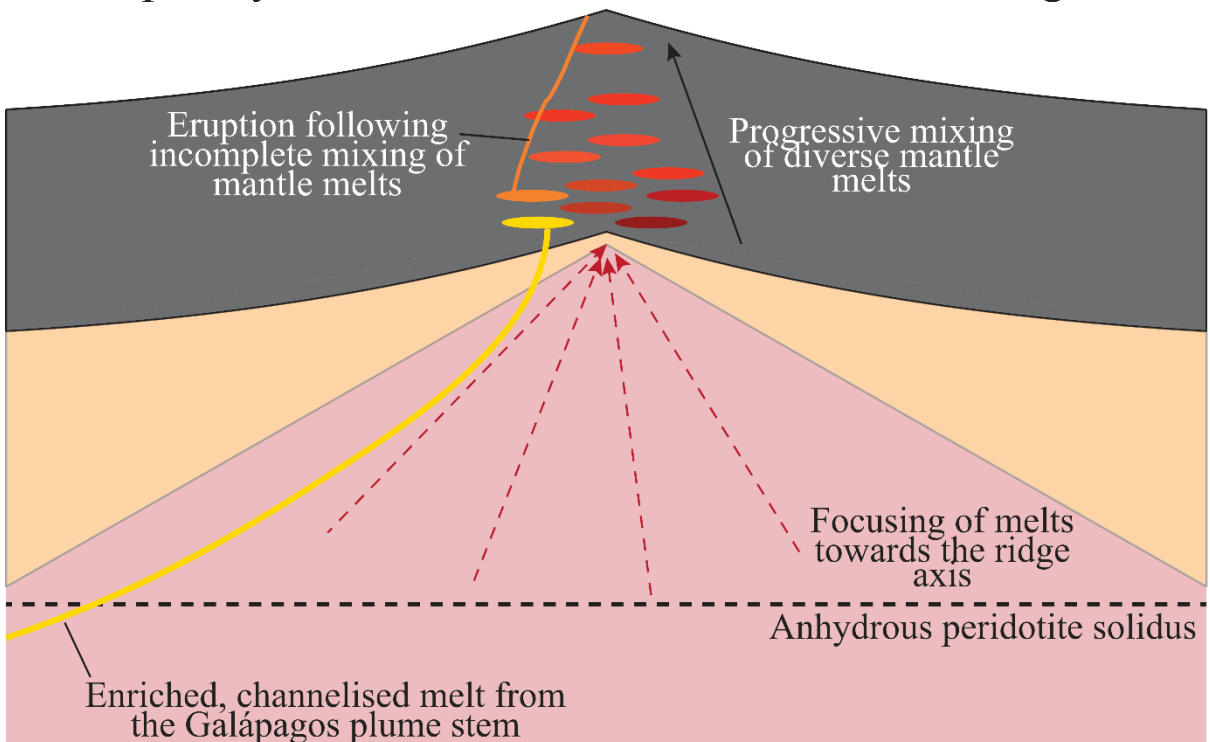
1264

1265 **Figure 7** – Comparison of our mantle melting models that include a contribution of plume-derived
1266 channelised melts to the composition of the anomalously enriched basalts from the GSC. **A.**
1267 composition of basalts that cannot be reproduced by our along-ridge models of plume-ridge
1268 interaction are shown in green and are generally characterised by $[H_2O]_{(8)}$ contents above 0.4 wt%.
1269 The composition of these enriched basalts is best reproduced when the proportion of channelised
1270 melt is >15% and the depth of channel formation is >3.2 GPa. Notably, as the pymelt simulations do
1271 not account for the presence of H_2O on the pyroxenite solidus, parameterisation of hydrous melting
1272 might influence our estimates for the pressure of channel formation. **B.** Comparison of 676 models
1273 to the composition of the TR164 6D-1g and TR164 6D-2g basalts (89.59 °W). The models with the
1274 lowest RMSE are shown by the darker colours. **C.** RMSE for all models shown in **B.** where the
1275 contribution of channelised melt is between 0 and 50%, and the pressure of channel formation is
1276 between 2.8 and 3.6 GPa. In all models the composition of the channelised melts are calculated
1277 using a T_p of 1400 °C and a pyroxenite source fraction of 20% (Gleeson et al. 2021).

Scenario 1: anomalously high delivery of channelised melt leads to crustal thickness anomaly.



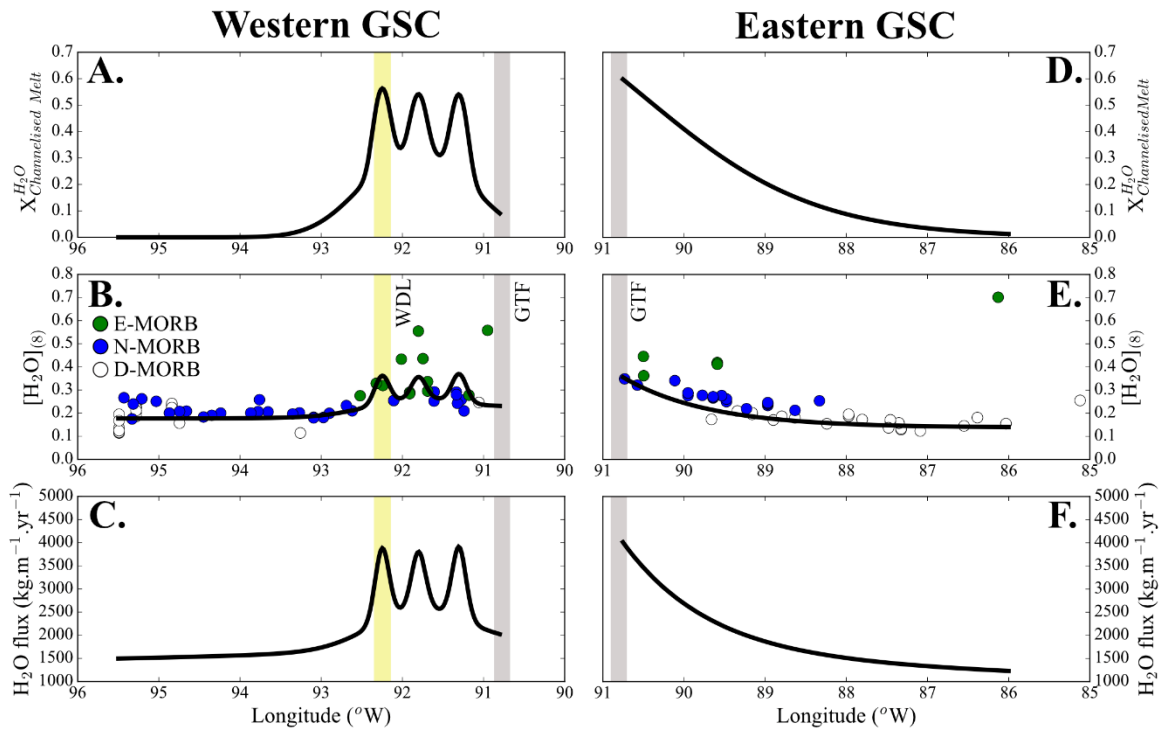
Scenario 2: Melts derived from the Galapagos plume stem incompletely mix with melts formed beneath the ridge axis.



This represents a post-print of a peer-reviewed manuscript that has been accepted for publication in *Geochemistry, Geophysics, Geosystems* (acceptance date 19/10/2021).

1279 **Figure 8** – Schematic diagram displaying the two ways in which delivery of channelised melt might
1280 contribute to the geochemical and geophysical parameters (such as crustal thickness) observed
1281 along the GSC. In Scenario 1, an anomalously high flux of channelised melt to the GSC results in
1282 moderately-to-highly enriched basalts at the surface and anomalously thick crust (e.g. at the
1283 intersection of the WDL with the GSC). In scenario 2, only a moderate supply of channelised melt
1284 exists. However, some of this channelised melt manages to ascend and erupt without completely
1285 mixing and/or homogenising with melts formed beneath the ridge axis leading to the presence of
1286 anomalously enriched basalts at the surface.

1287



1288

1289 **Figure 9** – H₂O concentrations and fluxes predicted by new models of plume-ridge interaction in the
 1290 Galápagos (models are identical to those shown in Fig. 5). The model accurately recreates the H₂O
 1291 contents of basalts from both the eastern GSC and the western GSC (model results assume ~20%
 1292 fractionation of olivine and/or plagioclase). The maximum outflux of H₂O along the western GSC is
 1293 ~4000 kg.m⁻¹.yr⁻¹ where the volcanic lineaments intersect the GSC (compared to the background flux
 1294 of only ~2000 kg.m⁻¹.yr⁻¹). The greatest outflux of H₂O from the GSC is observed on the eastern GSC
 1295 near the GTF (~4000 kg.m⁻¹.yr⁻¹) and, in this location, ~60% of the H₂O flux out of the GSC is sourced
 1296 from plume-derived channelized melts.

1297 **Table 1** – Parameters used in the solid-state and melt channelisation models of plume-ridge
 1298 interaction (shown in Figures 4 and 5, respectively).

Parameter	Solid State models		Melt channelisation models	
	Western GSC	Eastern GSC	Western GSC	Eastern GSC
T_p at GTF (°C)	1370	1375	1372	1387
T_p distal from GTF (°C)	1360	1365	1362	1365
U_{r-max} at GTF	7	8	2.5	1.8
A ^a	0.6	0.5	0.6	0.4
B ^a	6	8	1.5	0.8
C ^a	0	0	0	0
X_{Pyx}	0.10	0.10	0.06	0.08
A	0.4	0.4	0.4	0.3
B	0.08	0.09	0.04	0.06
C	0.02	0.01	0.02	0.02
$P_{termination}$ (GPa)^b at GTF	0.65	0.7	0.43	0.6
A	1.5	1.5	1.5	1.2
B	0.40	0.45	0.18	0.35
C	0.25	0.25	0.25	0.25
H₂O (peridotite)	145	100	145	100
H₂O (pyroxenite)	550	550	550	550
T_p for generation of channelised melts	n/a	n/a	1400	1400

1299 ^a U_{r-max} , X_{Pyx} , and $P_{termination}$ are calculated according to $(U_{r-max}, X_{Pyx}, P_{termination}) =$
 1300 $\exp\left(-\left((Long(^{\circ}W) - 90.8) \times A\right)\right) \times B + C$ on the western GSC and
 1301 $(U_{r-max}, X_{Pyx}, P_{termination}) = \exp\left(-\left((90.8 - Long(^{\circ}W)) \times A\right)\right) \times B + C$ on the eastern GSC.

1302 ^b $P_{termination}$ (GPa) refers to the pressure at the top of the melt column.

1303